

The First Maps of κ_d – the Dust Mass Absorption Coefficient – in Nearby Galaxies, with DustPedia

C. J. R. Clark¹, P. De Vis², M. Baes³, S. Bianchi⁴, V. Casasola⁴, L. P. Cassarà^{5,6}, J. I. Davies², W. Dobbels³, S. Lianou, I. De Looze^{3,7}, R. Evans², M. Galametz⁸, F. Galliano⁸, A. P. Jones⁹, S. C. Madden⁸, A. V. Mosenkov¹⁰, S. Verstocken³, S. Viaene^{3,11}, E. M. Xilouris¹², N. Ysard⁹

¹ Space Telescope Science Institute, 3700 San Martin Drive, Baltimore, Maryland, 21218, USA

² School of Physics & Astronomy, Cardiff University, Queen's Buildings, The Parade, Cardiff, CF24 3AA, UK

³ Sterrenkundig Observatorium, Universiteit Gent, Krijgslaan 281 S9, B-9000 Gent, Belgium

⁴ INAF, Osservatorio Astrofisico di Arcetri, Largo E. Fermi 5, I-50125, Florence, Italy

⁵ INAF, Istituto di Radioastronomia, Via Piero Gobetti 101, I-40127, Bologna, Italy

⁶ NAF-IASF Milano, Via Alfonso Corti 12, 20133, Milano, Italy

⁷ Department of Physics & Astronomy, University College London, Gower Street, London, WC1E 6BT, UK

⁸ AIM, CEA, CNRS, Université Paris-Saclay, Université Paris Diderot, Sorbonne Paris Cité, F-91191 Gif-sur-Yvette, France

⁹ Institut d'Astrophysique Spatiale, CNRS, Université Paris-Sud, Université Paris-Saclay, Bât. 121, 91405, Orsay Cedex, France

¹⁰ Central Astronomical Observatory of RAS, Pulkovskoye Chaussee 65/1, 196140, St. Petersburg, Russia

¹¹ Centre for Astrophysics Research, University of Hertfordshire, College Lane, Hatfield, AL10 9AB, UK

¹² National Observatory of Athens, Institute for Astronomy, Astrophysics, Space Applications and Remote Sensing, Ioannou Metaxa and Vasileos Pavlou GR-15236, Athens, Greece

* cclark@stsci.edu

ABSTRACT

The dust mass absorption coefficient, κ_d is the conversion function used to infer physical dust masses from observations of dust emission. However, it is notoriously poorly constrained, and it is highly uncertain how it varies, either between or within galaxies. Here we present the results of a proof-of concept study, using the DustPedia data for two nearby face-on spiral galaxies M 74 (NGC 628) and M 83 (NGC 5236), to create the first ever maps of κ_d in galaxies. We determine κ_d using an empirical method that exploits the fact that the dust-to-metals ratio of the interstellar medium is constrained by direct measurements of the depletion of gas-phase metals. We apply this method pixel-by-pixel within M 74 and M 83, to create maps of κ_d . We also demonstrate a novel method of producing metallicity maps for galaxies with irregularly-sampled measurements, using the machine learning technique of Gaussian process regression. We find strong evidence for significant variation in κ_d . We find values of κ_d at 500 μm spanning the range 0.11–0.25 $\text{m}^2 \text{kg}^{-1}$ in M 74, and 0.15–0.80 $\text{m}^2 \text{kg}^{-1}$ in M 83. Surprisingly, we find that κ_d shows a distinct inverse correlation with the local density of the interstellar medium. This inverse correlation is the opposite of what is predicted by standard dust models. However, we find this relationship to be robust against a large range of changes to our method – only the adoption of unphysical or highly unusual assumptions would be able to suppress it.

Key words: galaxies: ISM – galaxies: general – ISM: dust – ISM: abundances – submillimetre: ISM – methods: observational

1 INTRODUCTION

Interstellar dust provides an indispensable window for studying galaxies and their evolution. Dust, which primarily emits in the Mid-Infrared (MIR) to Far-Infrared (FIR) to submillimetre (submm) wavelength regime, can be observed in very large numbers of galaxies very rapidly, with the ben-

eficial effects of negative k -correction enhancing our ability to detect dusty galaxies out to high redshift (Eales et al. 2010a; Oliver et al. 2012). This has made dust a standard proxy for studying galaxies' star-formation (Kennicutt 1998; Buat et al. 2005; Kennicutt et al. 2009), gas mass (Eales et al. 2012; Scoville et al. 2014; Lianou et al. 2016), and chemical evolution (Rowlands et al. 2014; Zhukovska 2014;

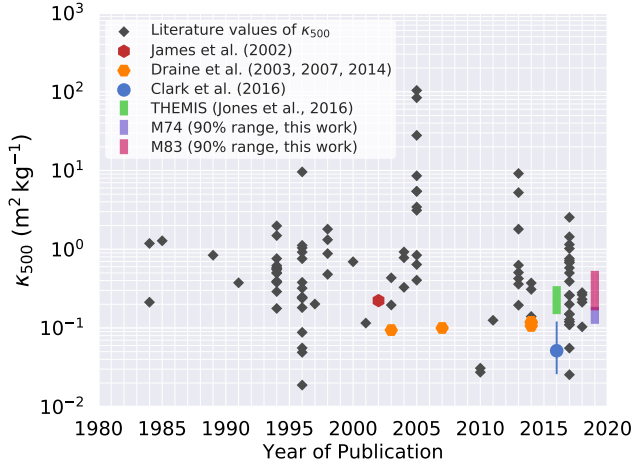


Figure 1. Literature values of κ_{500} , plotted against the year in which they were published. This is an updated version of Figure 1 from Clark et al. (2016), revised to include values published subsequent to that work, plus additional historical values. A full list of references for the plotted values is provided as a footnote to this figure^a. All values were converted to the 500 μm reference wavelength^b according to Equation 2, assuming^c $\beta = 2$. Several prominent values have been highlighted. Rectangular markers indicate the range encompassed by a particular set of values. The 5th–95th percentile ranges we find for M83 and M74 in this work are also plotted, for later reference (with the overlap between their ranges correspondingly shaded).

^a The plotted values of κ_d include the values given in the compilation tables of Alton et al. (2004) and Demyk et al. (2013), along with the values reported by: Ossenkopf & Henning (1994); Agladze et al. (1996); Weingartner & Draine (2001); James et al. (2002); Draine (2003); Dasyra et al. (2005); Draine & Li (2007); Eales et al. (2010b); Ormel et al. (2011); Compiègne et al. (2011); Draine et al. (2014); Gordon et al. (2014); Planck Collaboration et al. (2014); Köhler et al. (2015); Jones et al. (2016); Roman-Duval et al. (2017); Bianchi et al. (2017); Demyk et al. (2017a,b); Chiang et al. (2018).

^b The choice of reference wavelength has negligible (< 0.1 dex) effect on the standard deviation of the literature κ_d values in the plot, as long as $100 < \lambda_0 < 1000 \mu\text{m}$.

^c Changing β to any value in the standard range of 1–1.5 has negligible (< 0.05 dex) effect on the standard deviation of the literature κ_d values in the plot.

De Vis et al. 2017a,b, 2019) – which are otherwise difficult and time-consuming to observe directly.

However, many of the valuable insights that dust can provide rest upon one simple expectation – that we are able to use observations of dust emission to actually infer physical dust masses. Unfortunately, astronomers remain *terrible* at this. This is due to the fact that κ_d (variously called the dust mass absorption coefficient, or the dust mass opacity coefficient), the wavelength-dependent conversion factor used to calculate dust masses from FIR–submm dust Spectral Energy Distributions (SEDs), is extremely poorly constrained.

κ_d is essentially a convenience factor, amalgamating the various properties of dust grains that dictate their emissivity – such as the distributions of size, morphology, density, and chemical composition. These individual properties are extremely hard to constrain observationally, and highly degenerate with each other in their effect upon dust emission

(Whittet 1992); combining them in κ_d allows them to be considered in terms of their net effect. Dust emission in the FIR–submm regime is traditionally modelled as a Modified BlackBody (MBB; or, ‘greybody’), where the observed flux density S_λ at wavelength λ is described by:

$$S_\lambda = \frac{1}{D^2} \sum_i^n M_i \kappa_{\lambda_i} B(\lambda, T_i) \quad (1)$$

where D is the distance to the source of the dust emission, n is the number of dust components being modelled, M_i is the mass of dust component i , κ_{λ_i} is the value of κ_d at wavelength λ for dust component i , and $B_\lambda(T_i)$ is the Planck function evaluated at wavelength λ for temperature T_i of dust component i . While the dust population of a source will in reality span a continuum of temperatures, availability of FIR–submm data typically forces observers to fit their data with only 1 or 2 components (although point-process methods are starting to provide a way to model dust in a more continuous manner; see Marsh et al. 2015, 2017).

The value of κ_d can be estimated in various ways, usually by some combination of: consideration of the elemental constituents of dust (derived from depletions); physical modelling of possible grain structures; chemical modelling of likely dust compositions; radiative transfer modelling; analysis of Ultraviolet (UV) to Near-Infra-Red (NIR) extinction and scattering; laboratory analysis of artificial dust grain analogues; and examination of retrieved grains of interplanetary and interstellar dust. For a fuller summary, and compilation of references, see Section 1 of Clark et al. (2016). Troublingly, the various methods that have been employed for estimating κ_d yield a very wide range of possible values. In order to directly compare different values of κ_d , they need to be converted to the same reference wavelength. This can be done using the formula:

$$\kappa_\lambda = \kappa_0 \left(\frac{\lambda_0}{\lambda} \right)^\beta \quad (2)$$

where κ_λ is the value of κ_d at a particular wavelength λ , κ_0 is the value of κ_d at a reference wavelength λ_0 , and β is the dust emissivity spectral index. Laboratory analysis of dust analogues and chemical modelling suggest that this relation is reliable in the wavelength range $150 \lesssim \lambda \lesssim 1000 \mu\text{m}$; at wavelengths shorter than this the variation of κ_d with wavelength becomes much more complex, whilst at longer wavelengths the behaviour of κ_d is less clear, with some evidence of an upturn (Demyk et al. 2017a,b; Ysard et al. 2018).

Figure 1 compiles a wide range of κ_d values that have been reported in the literature (all have been converted to a reference wavelength of 500 μm as per Equation 2; we only plot values for which the original quoted reference wavelength was in the reliable 150–1000 μm range). Over 100 values are plotted, with a standard deviation of 0.8 dex, and spanning a total range of over 3.6 orders of magnitude. Worse still, there is no sign that values of κ_d reported in the literature are converging over time.

So, despite the excellent sensitivity and wavelength coverage provided by modern FIR–mm observatories, any dust masses inferred from observed dust emission remain enormously uncertain, stymieing our understanding of the Inter-Stellar Medium (ISM) in galaxies. Moreover, this high degree of uncertainty means that, out of necessity, κ_d is often treated as being constant – even though it is well understood

that this can't be true in reality. Even the more complex, multi-phase dust model frameworks, such as those of Jones et al. (2013, 2017), usually only incorporate 2 or 3 types of dust, each with a corresponding κ_d .

As such, understanding how kappa varies – both between different galaxies, and within individual galaxies – is clearly vital for the field.

In this paper, we use an empirical method for determining the value of κ_d – which we employ on a resolved, pixel-by-pixel basis in two nearby galaxies – to produce the first maps of how κ_d varies within galaxies, as a proof-of-concept study. The theory behind the dust-to-metals method we employ to find κ_d is described in Section 2. The galaxies and data we use in this work are described in Section 3. The application of the technique to produce maps of κ_d is Section 4. Our results are presented in Section 5, and are discussed in Section 6. For brevity and readability, ‘flux density’ will be termed ‘flux’ throughout the rest of the paper.

2 THEORY

Of the many methods proposed for estimating the value of κ_d , one of the most simple is that first proposed by James et al. (2002). The James et al. (2002) method is entirely empirical, and relies upon just one central assumption – that the dust-to-metals ratio in the ISM, ϵ_d , has a known value. If the ISM mass of a galaxy is known, along with the metallicity of that ISM, it is straightforward to calculate the total mass of interstellar metals in that galaxy; then, by assuming a fixed dust-to-metals ratio, it is possible to infer a galaxy's dust mass *a priori*, without any reference to the dust emission. This *a priori* dust mass can then be compared to that galaxy's observed dust emission, and hence κ_d can be calibrated. Here we use the ϵ_d notation for the dust-to-metals ratio, instead of \mathcal{DTM} . This maintains consistency with James et al. (2002) and Clark et al. (2016), and avoids any ambiguity arising from the fact that \mathcal{DTM} is often used to denote a dust-to-metals ratio *normalised by the Milky Way value*, whereas our quoted dust-to-metals ratios are always absolute values.

The vast majority of all reported values of ϵ_d lie in the range 0.2–0.6 (considering only values of ϵ_d that are not based upon some assumed value of κ_d : Issa et al. 1990; Luck & Lambert 1992; Whittet 1992; Pei 1992; Meyer et al. 1998; Dwek 1998; Pei et al. 1999; Weingartner & Draine 2001; James et al. 2002; Kimura et al. 2003; Draine et al. 2007; Jenkins 2009; Peeples et al. 2014; McKinnon et al. 2016; Wiseman et al. 2017; Telford et al. 2018). As such, it seems fair to conclude that ϵ_d is significantly better constrained than κ_d – making the former a useful tool for pinning down the value of the latter. And whilst some authors suggest larger values of ϵ_d (for instance De Cia et al. 2013, who find values in the region of 0.8), we can at least be confident that, by definition, no galaxy has a dust-to-metals ratio greater than 1 – no such helpful constraint exists for κ_d . Furthermore, thanks to observations of elemental depletions in the neutral ISM, ϵ_d can be determined far more directly than κ_d .

Clark et al. (2016) built upon the James et al. (2002) method, to correct for a number of systematics that affected that original implementation, and to enable it to take ad-

vantage of higher-quality modern FIR–submm data. In this work, we apply the Clark et al. (2016) iteration of the dust-to-metals method on a resolved basis, in nearby galaxies. Therefore, for completeness, we here provide a cursory description of the technique as implemented in this work; for a full derivation and description, refer to Section 2 of Clark et al. (2016). The final form of the method can be rendered as the following formula for computing κ_λ for the ISM of a source:

$$\kappa_\lambda = \frac{D^2}{\xi (M_{\text{HI}} + M_{\text{H}_2}) \epsilon_d f_Z} \sum_i^n \left(\frac{S_{\lambda_i}}{B_\lambda(T_i)} \right)_i \quad (3)$$

where ξ is a correction factor to account for the fraction of ISM mass due to elements other than hydrogen, M_{HI} is the atomic hydrogen mass, M_{H_2} is the molecular hydrogen mass, ϵ_d is the dust-to-metals ratio, and f_Z is the ISM metal mass fraction. The $\sum_i^n \left(\frac{S_{\lambda_i}}{B_\lambda(T_i)} \right)_i$ term corresponds to the model used to fit the observed dust emission of the target source – in this instance, n MBBs, as per Equation 1; n is the number of dust components being modelled, S_{λ_i} is the flux emitted at wavelength λ by dust component i , and $B_\lambda(T_i)$ is the Planck function evaluated at wavelength λ for temperature T_i of dust component i ; our SED-fitting procedure is described in Section 4.2.

The formulation in Equation 3 gives a combined κ_d value, that incorporates the contribution from all dust species present, for each temperature component (for $n > 1$). The problem becomes unconstrained if each dust component is treated as having a different κ_d . The potential impact of line-of-sight mixing of dust components at different temperatures is discussed in Section 4.2.

The correction factor ξ is required in Equation 3, as the dust-to-metals method is concerned with the *total* mass of the ISM, not just the mass of hydrogen. It is standard in the literature to account for mass other than hydrogen by applying a fixed factor of 1.36 – corresponding to the Milky Way helium abundance. However this fails to consider how helium abundance varies with galaxy evolution, or the contribution of metals to the mass of the ISM. Thus ξ is defined as:

$$\xi = \frac{1}{1 - \left(f_{\text{He}_p} + f_Z \left[\frac{\Delta f_{\text{He}}}{\Delta f_Z} \right] \right) - f_Z} \quad (4)$$

where f_{He_p} is the primordial helium mass fraction, and $\left[\frac{\Delta f_{\text{He}}}{\Delta f_Z} \right]$ describes the evolution of the helium mass fraction with metallicity. We use $f_{\text{He}_p} = 0.2485 \pm 0.0002$ from Aver et al. (2013), and $\left[\frac{\Delta f_{\text{He}}}{\Delta f_Z} \right] = 1.41 \pm 0.62$ from Balser (2006). Given Equation 4, ξ can therefore vary from 1.33 (for low-metallicity galaxies where $Z \rightarrow 0$) to 1.45 (for high-metallicity giant ellipticals where $Z = 1.5Z_\odot$).

It is important to note that $12 + \log_{10} \left[\frac{\text{O}}{\text{H}} \right]$ measurements trace gas-phase metallicity in the ionised phase (predominantly HII regions), whereas we are concerned with the metallicity of the ISM at large. This means that we must account for the fraction of interstellar oxygen mass in HII regions depleted onto dust grains, δ_{O} , and hence missed by gas-phase metallicity estimators. We use a value of $\delta_{\text{O}} = 1.32 \pm 0.09$ from Mesa-Delgado et al. (2009), which is in good agreement with numerous other reported values (Peimbert & Peimbert 2010; Kudritzki et al. 2012; Bresolin et al. 2016). Whilst the oxygen depletion factor in the ISM at large

is known to vary by at least 0.3 dex (Jenkins 2009), oxygen depletion in HII regions is found to be remarkably constant, at ~ 1.3 (ie, ~ 0.1 dex) across nearby galaxies (evaluated by comparing abundances in HII regions to abundances in the atmospheres of nearby B stars; Bresolin et al. 2016 and references therein). Additionally, given that the elemental composition of oxygen-rich dust is found to exhibit minimal variation at intermediate-to-high metallicities (Mattsson et al. 2019), the assumption of a constant δ_O is valid modulo a constant ϵ_d – which is the central premise of our method.

Atomic hydrogen mass, M_{HI} (in M_\odot), is determined using observations of the 21 cm hyperfine structure line, according to the standard prescription:

$$M_{\text{HI}} = 2.356 \times 10^{-7} S_{\text{HI}} D^2 \quad (5)$$

where S_{HI} is the velocity-integrated flux density of the 21 cm line (in Jy km s^{-1}), and the source distance D is here in units of pc.

The mass of molecular hydrogen associated with a source cannot be determined directly from emission; because the H_2 molecule is non-polar, it does not radiate when in the ground state (which is the case for the bulk of molecular hydrogen in galaxies). Instead, molecular hydrogen masses are typically inferred by treating CO as a tracer molecule, via observations of the $^{12}\text{C}^{16}\text{O}(1-0)$ rotational line (referred to as CO(1-0) hereafter). The mass of molecular hydrogen, M_{H_2} (in M_\odot), can thus be calculated using the relation:

$$M_{\text{H}_2} = I_{\text{CO}} \alpha_{\text{CO}} (2 D \tan\left(\frac{\theta}{2}\right))^2 \quad (6)$$

where I_{CO} is the velocity-integrated main-beam brightness temperature of the CO(1-0) line (in K km s^{-1}), α_{CO} is the CO-to- H_2 conversion factor (in $M_\odot \text{Jy}^{-1} \text{km}^{-1} \text{s}$), θ is the angular diameter of the target source, and the source distance D is here in units of pc. The value of α_{CO} is a matter of much debate, but the standard Milky Way value is $\alpha_{\text{CO,MW}} = 3.2 \text{ K}^{-1} \text{ km}^{-1} \text{ s pc}^{-2}$, which is treated as uncertain by a factor of 2 (see Obreschkow & Rawlings 2009, Saintonge et al. 2011, Bolatto et al. 2013, and references therein). Note that Equation 6 is simply the standard H_2 mass surface-density prescription, $\Sigma_{\text{H}_2} = I_{\text{CO}} \alpha_{\text{CO}}$ (where Σ_{H_2} is in units of $M_\odot \text{pc}^2$), rendered in terms of M_{H_2} for consistency with Equations 3 and 5. The CO-to- H_2 conversion factor can alternatively be expressed as X_{CO} , which is in terms of column number density density of molecules, being related to α_{CO} according to $X_{\text{CO}} = 6.3 \times 10^{19} \alpha_{\text{CO}}$.

The galaxies considered in this work contain environments with metallicities that vary by a factor of 2.5, spanning 0.4–1 Z_\odot (see Section 4). When considering locales with significantly-varying metallicities, it is important to account for the corresponding variation of α_{CO} with metallicity (Bolatto et al. 2013). In lower-metallicity environments, there will be reduced abundances of C and O, relative to H. Additionally, there is less dust available in low-metallicity environments to shield the CO – which is less able to self-shield than H_2 – from photodissociation (see Wolfire et al. 2010, Clark & Glover 2015, and references therein). Here we opt to use the metallicity-dependent α_{CO} prescription of Amorín et al. (2016), described by:

$$\alpha_{\text{CO}} = \alpha_{\text{CO,MW}} \left(\frac{Z}{Z_\odot} \right)^{-y_{\text{CO}}} \quad (7)$$

where $\frac{Z}{Z_\odot}$ is the ISM metallicity in terms of the Solar value, and y_{CO} is an empirical power-law index with a value of 1.5 ± 0.3 .

The Amorín et al. (2016) rule is calibrated on a sample of galaxies spanning over an order of magnitude in metallicity ($7.69 < 12 + \log_{10}[\frac{\text{O}}{\text{H}}] < 8.74$), by using the Star Formation Efficiency (SFE) and Star Formation Rate (SFR) to infer the molecular gas supply present. They do this by employing the relation $\frac{\alpha_{\text{CO}}}{\alpha_{\text{CO,MW}}} = \tau_{\text{H}_2} \frac{\text{SFR}}{M_{\text{H}_2}}$; effectively inverting the Kennicutt-Schmidt law (Kennicutt 1998) to infer the molecular gas mass present, anchored by the known star formation efficiency of the Milky Way. Resolved studies such as Bigiel et al. (2011) and Utomo et al. (2019) find remarkably little variation in SFE within face-on local normal spirals like those studied in this work; this supports the reliability of using a SFE-calibrated method for estimating α_{CO} in a resolved study such as ours. Additionally, the Amorín et al. (2016) prescription effectively traces the median of the commonly-cited metallicity-dependent literature prescriptions (see Figure 11 of Amorín et al. 2016 and Figure 6 of Accurso et al. 2017 for comparisons of prescriptions), making it the choice most likely to not conflict with other works.

Regarding the Solar metallicity, we use the canonical value for the Solar oxygen abundance of $[12 + \log_{10} \frac{\text{O}}{\text{H}}]_\odot = 8.69 \pm 0.05$ (Asplund et al. 2009), corresponding to a Solar metal mass fraction of $f_{Z_\odot} = 0.0134$ (Asplund et al. 2009, uncertainty deemed to be negligible). In common with the literature at large, we assume that oxygen abundance traces total metallicity. Whilst this assumption has its limits, oxygen is the most abundant metal in the Universe, and a dominant constituent of dust (Savage & Sembach 1996; Jenkins 2009), making it a useful metallicity tracer for our purposes. Although the ratio of oxygen to carbon (the other main constituent of dust by mass) is known to vary with metallicity (Garnett et al. 1995), this systematic trend is no more prominent than the intrinsic scatter over the 0.4–1.0 Z_\odot metallicity range relevant to this work (Pettini et al. 2008; Berg et al. 2016).

Although a D^2 term appears in Equation 3, the M_{HI} and M_{H_2} terms are also both proportional to D^2 , which therefore ultimately cancels out. This renders the resulting values of κ_λ independent of distance, removing a potentially large source of uncertainty.

Throughout this work, when employing values from the literature, we take care to only use values that do not themselves rely upon any assumed value of κ_d .

For the value of the dust-to-metals ratio, ϵ_d , in Equation 3, we take two approaches. For our fiducial analysis, presented in Section 5, we assume a constant value of $\epsilon_d = 0.4 \pm 0.2$. This is smaller than the value of 0.5 assumed in Clark et al. (2016), as more recent works (McKinnon et al. 2016; De Cia et al. 2016; Wiseman et al. 2017) suggest that for most galaxies with metallicities $> 0.1 Z_\odot$, the dust-to-metals ratio is slightly below the Milky Way’s average value of 0.5 (James et al. 2002; Jenkins 2009).

The assumption of a constant dust-to-metals ratio is an approximation that will break down at some point. Therefore, in Section 6.2.1, we construct an alternate analysis where ϵ_d increases as a function of ISM surface density. This is a more physical treatment, as depletion of ISM metals onto

Table 1. Basic properties of M 74 and M 83, the galaxies studied in this work. All values derived from the data presented in [Clark et al. \(2018\)](#), unless otherwise specified.

	M 74	M 83
NGC N ^o	NGC 628	NGC 5236
RA (J2000)	24.174° (01 ^h 36 ^m 41 ^s 8)	204.254° (13 ^h 37 ^m 01 ^s 0)
Dec (J2000)	+15.783° (+15° 46′ 58″ 8)	-29.866° (-29° 51′ 57″ 6)
Distance (Mpc) ^a	10.1	4.9
Hubble Type	SAC (5.2)	SBc (5.0)
D_{25} (arcmin)	10.0	13.5
D_{25} (kpc)	29.4	19.2
A_{25} (kpc ²)	683	290
M_* ($\log_{10} M_\odot$) ^b	10.1	10.5
M_{HI} ($\log_{10} M_\odot$) ^c	9.9	10.0
M_{H_2} ($\log_{10} M_\odot$) ^d	9.4	9.5
M_d ($\log_{10} M_\odot$) ^e	7.5	7.4
SFR ($M_\odot \text{ yr}^{-1}$) ^b	2.4	6.7
FUV- K_S (mag)	2.9	3.4
NUV- r (mag)	2.5	2.8

^a As a first-order estimate of the uncertainty on the distance, we use the standard deviation of the redshift-independent distances listed in the NASA/IPAC Extragalactic Database (NED; <https://ned.ipac.caltech.edu/ui/>) for each galaxy. This gives uncertainties of 3.2 and 3.4 Mpc for M 74 and M 83 respectively.

^b [Nersesian et al. \(2019\)](#).

^c HI mass from total single-dish flux in the HI Parkes All Sky Survey (HIPASS; [Meyer et al. 2004](#); [Wong et al. 2006](#)).

^d This work (see Section 3.4).

^e This work (using the pixel-by-pixel κ_d values calculated in produced 5).

dust grains is found to increase in regions of greater ISM column density ([Jenkins 2009](#); [Roman-Duval et al. 2019](#)). This is in agreement with the fact that grain growth in the ISM is required to explain the dust budgets in many galaxies ([Galiano et al. 2008](#); [Rowlands et al. 2014](#); [Zhukovska 2014](#)). As a result, dust grain growth in denser ISM (with the corresponding increase in ϵ_d) is a feature of dust evolution models such as The Heterogeneous dust Evolution Model for Interstellar Solids (THEMIS; [Jones et al. 2013, 2017](#); [Jones 2018](#)). Unfortunately, the exact form of the relationship between ϵ_d and ISM (surface) density is very poorly constrained (the relationship we assume for our analysis is described in detail in Section 6). As such, the variable- ϵ_d model represents a more-physical, but worse-constrained approach; whilst the fixed- ϵ_d model represents a less-physical, but better-constrained approach. For this reason, whilst the fixed- ϵ_d approach is our fiducial model, we nonetheless consider both scenarios.

3 DATA

An initial attempt by [Clark et al. \(2016\)](#) to detect variation in κ_d using the dust-to-metals method was unsuccessful; however, that study only considered the global dust properties of galaxies, and considered a sample of 22 objects, all of which were of similar masses, metallicities, and environments. A promising avenue for finding variation in κ_d is to look *within* well-resolved nearby galaxies. Many studies

have found that dust properties can vary significantly – and sometimes dramatically – within galaxies ([Smith et al. 2012](#); [Roman-Duval et al. 2017](#); [Relaño et al. 2018](#)). It would be surprising if this variation did not extend to κ_d .

Creating a κ_d map of a galaxy using the dust-to-metals method requires resolved data for its dust emission, atomic gas, molecular gas, and metallicity; with the resolution provided by modern observations, it is possible to make many hundreds, or even thousands, of independent κ_d determinations within a galaxy. For this proof-of-concept demonstration we map κ_d within two nearby face-on spiral galaxies – M 74 (NGC 628) and M 83 (NGC 5236). We select these galaxies on account of their particularly extensive metallicity data (see Section 3.3), coupled with their resolution-matched multi-phase ISM observations (see Section 3.4).

We obtained the bulk of the necessary data from the DustPedia archive¹. DustPedia ([Davies et al. 2017](#)) is a European Union project working towards a comprehensive understanding of dust in the local Universe, capitalising on the legacy of the *Herschel* Space Observatory ([Pilbratt et al. 2010](#)). A centrepiece of the project is the DustPedia database, which includes every galaxy observed by *Herschel* that has recessional velocity within 3000 km s^{-1} ($\sim 40 \text{ Mpc}$), has optical angular size in the range $1' < D_{25} < 1^\circ$, and has a detected stellar component².

The continuum data we employ is described in Section 3.2, the metallicity data (and the process by which we use it to create metallicity maps) is described in Section 3.3, and the atomic & molecular gas data in Section 3.4.

3.1 Target Galaxies

We selected M 74 and M 83 as the subject galaxies for this work; a summary of their basic characteristics is provided in Table 1. Both are very nearby, highly extended, and almost perfectly face-on, making them two of the most heavily-studied galaxies in the sky, and ideally suited to serving as our proof-of-concept targets for mapping κ_d .

Both galaxies are classified as ‘grand design’ ([Elmegreen & Elmegreen 1987](#)) type Sc spirals, with M 83 also displaying a prominent bar ([de Vaucouleurs et al. 1991](#)). M 74 has a physical diameter of 29 kpc – similar to that of the Milky Way ([Goodwin et al. 1998](#); [Rix & Bovy 2013](#)) – and about 50% greater than that of M 83 (diameter defined according to the optical D_{25} , being the isophotal major axis at which the optical surface brightness falls beneath 25 mag arcsec²).

Despite being the physically smaller of the two, M 83 has a stellar mass 2.2 times greater, and a Star Formation Rate (SFR) 2.7 times greater ([Nersesian et al. 2019](#)). M 83 has a correspondingly higher surface brightness in dust emission, averaging 4.2 MJy sr^{-1} at $500 \mu\text{m}$ within its D_{25} , compared to 1.6 MJy sr^{-1} for M 74. The nuclear region of M 83 is currently undergoing a bar-driven starburst, concentrated in the central 250 pc, accounting for $\sim 10\%$ of the galaxy’s total ongoing star-formation ([Sérsic & Pastoriza](#)

¹ <https://dustpedia.astro.noa.gr/>

² As defined according to detection by the Wide-Field Infrared Survey Explorer (WISE; [Wright et al. 2010](#)), at its all-sky sensitivity, in $3.4 \mu\text{m}$ (its most sensitive band).

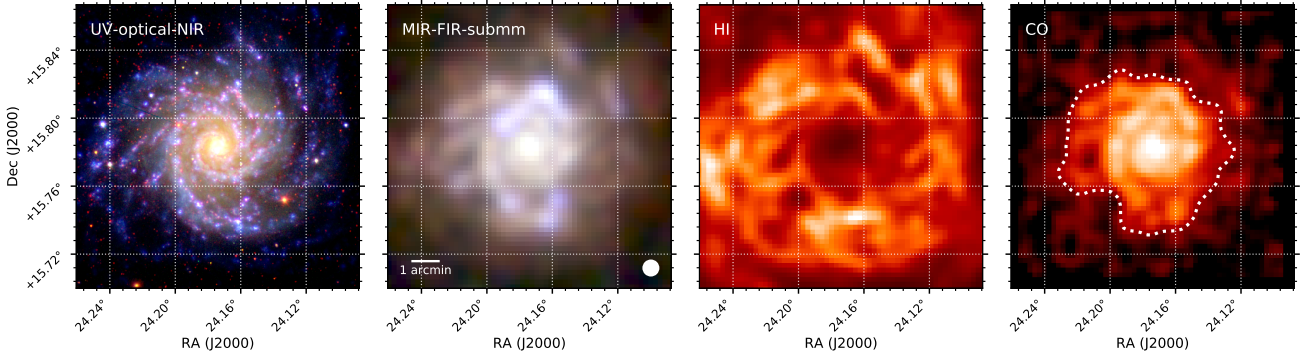


Figure 2. Multiwavelength overview of M74. *1st*: Three-colour UV-optical-NIR image, composed of GALEX NUV (blue), SDSS *g* (green), and *Spitzer*-IRAC 3.6 μm (red) data. *2nd*: Three-colour MIR-FIR-submm image, composed of WISE 22 μm (blue), *Herschel*-PACS 160 μm (green), and *Herschel*-SPIRE 350 μm (red) data. *3rd*: THINGS H I moment-0 map. *4th*: HERACLES CO(2-1) moment-0 map. Except for the UV-optical-NIR image, all maps are convolved to the 36'' limiting resolution at which we perform our analysis (beam size indicated in the 2nd panel). The dotted line in the far-right panel marks the SNR=2 contour of the CO(2-1) map, which is the region within which we mapped κ_d .

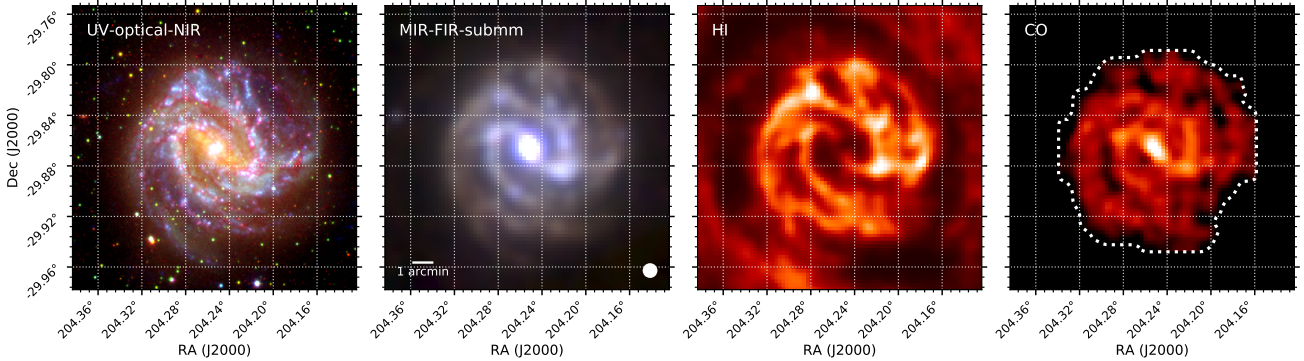


Figure 3. Multiwavelength overview of M83. Description as per Figure 2, with the exceptions that the green channel in the far-left three-colour UV-optical-NIR image corresponds to DSS *B*-band, the CO moment-0 map is SEST CO(1-0) data, and that the limiting resolution of our M83 data is 42'' (images convolved accordingly).

1965; Harris et al. 2001; Fathi et al. 2008). The optical disc of M83 has a minimal systematic metallicity gradient, with oxygen abundances varying by only about 0.1 dex from place to place; in contrast, M74 has a pronounced metallicity gradient, with oxygen abundances in its centre about 0.3 dex greater than at its R_{25} (De Vis et al. 2019).

Many of the differences between M74 and M83 – such as in their stellar surface densities (and therefore interstellar radiation fields), star formation characteristics, metallicity profiles, ISM distributions, etc – have the potential to affect dust properties, and thereby provide useful scope for us to contrast how κ_d can vary due to a range of factors.

The appearances of both galaxies, in various parts of the spectrum, are illustrated in Figures 2 and 3. The stellar masses and SFRs for the DustPedia galaxies, as presented in Nersesian et al. (2019), were estimated using the Code Investigating GALaxy Emission (CIGALE; Burgarella et al. 2005; Noll et al. 2009) software, incorporating the THEMIS dust model.

3.2 Continuum Data

Multiwavelength imagery and photometry for the DustPedia galaxies (spanning 42 ultraviolet–millimetre bands), along with distances, morphologies, etc, are presented in Clark et al. (2018). Our analysis makes use of observations from several of the facilities included in the DustPedia archive.

In the submm, we use observations at 250, 350, and 500 μm from the Spectral and Photometric Imaging Receiver (SPIRE; Griffin et al. 2010) instrument onboard *Herschel*. In the FIR, we use observations at 160, and 70 μm from the Photodetector Array Camera and Spectrometer (PACS; Poglitsch et al. 2010) instrument, also onboard *Herschel* (PACS did not perform 100 μm observations for M83, so for consistency we make no use of the the PACS 100 μm data for M74). In the MIR, we use observations at 22 μm from the WISE³. A compilation of the MIR-FIR-submm data for each galaxy is shown in the centre-left panels of Figures 2 and 3.

³ Whilst 24 μm *Spitzer* data does exist for these galaxies, the background is better-behaved in the WISE data, thanks to the superior mosaicing permitted by the larger field of view.

Although not required for the creation of the κ_d maps, we use various additional data for reference and comparison, also drawn from the DustPedia archive. This includes UltraViolet (UV) observations from GALaxy Evolution eXplorer (GALEX; Morrissey et al. 2007); UV, optical, and NIR observations from the Sloan Digital Sky Survey (SDSS; York et al. 2000; Eisenstein et al. 2011); optical observations from the Digitized Sky Survey (DSS); plus NIR observations from the InfraRed Array Camera (IRAC; Fazio et al. 2004) and Multiband Imager for *Spitzer* (MIPS; Rieke et al. 2004) instruments onboard the *Spitzer* Space Telescope (Werner et al. 2004). A compilation of the UV–optical–NIR data for each galaxy is shown in the far-left panels of Figures 2 and 3.

3.3 Metallicity Data

Galaxies sufficiently extended to have well-resolved global FIR–submm observations, atomic gas observations, and molecular gas observations, are generally *too* extended to have their UV–NIR nebular spectral emission – and hence metallicities – fully mapped by Integral Field Unit (IFU) spectrometry. Whilst some large-area IFU surveys of nearby galaxies have now been undertaken, these are still very much the exception rather than the rule, and even the very largest can currently only cover $\sim 50\%$ of the area of galaxies as extended as M74 and M83. (Rosales-Ortega et al. 2010; Sánchez et al. 2011; Blanc et al. 2013). As such, the few DustPedia galaxies with mostly complete IFU coverage do not have the well-resolved gas and dust data needed for this analysis.

However, extended nearby galaxies are popular targets for spectroscopic observation; most have had large numbers of individual slit and fibre spectra taken, supplementing partial IFU coverage like that described above. For DustPedia, De Vis et al. (2019) have compiled a sizeable database of emission line fluxes, collated from 42 literature studies plus all available archival Multi Unit Spectroscopic Explorer (MUSE; Bacon et al. 2010) data that covers the DustPedia galaxies. The De Vis et al. (2019) spectroscopic database contains emission line fluxes from 10,000 spectra, with data for 492 (56%) of the DustPedia galaxies. De Vis et al. (2019) also present consistent gas-phase metallicity measurements for all of these spectra, for 5 different strong-line relation prescriptions (all of which yield standard $12 + \log_{10}[\frac{O}{H}]$ metallicities). Following their tests of the internal consistency of the prescriptions considered, De Vis et al. (2019) find the Pilyugin & Grebel (2016) ‘S’ prescription most reliable; we therefore use these metallicities throughout the rest of this work. A recent study by Ho (2019) also supports the validity of the Pilyugin & Grebel (2016) prescriptions at the metallicities of our target galaxies. As an additional test, we also repeat the entire κ_d -mapping process using metallicity data produced using 4 other strong-line relations; this is presented in Appendix F.

M74 and M83 both have large numbers of metallicities in the De Vis et al. (2019) database – 510 and 793 measurements respectively, more than any other DustPedia galaxy (except UGC 09299, which lacks the resolved gas data we require). These metallicity points sample the entirety of both galaxies’ optical discs. The positions of these spectra, and the metallicities derived from them, are plotted in the

Table 2. Results of our modelling of the radial metallicity profiles of M74 and M83. Stated values are posterior medians, with uncertainties indicating the 68.3% credible interval (all posteriors were symmetric and Gaussian).

	M 74	M 83
m_Z (dex r_{25}^{-1})	-0.27 ± 0.04	-0.14 ± 0.02
c_Z ($12 + \log_{10}[\frac{O}{H}]$)	8.59 ± 0.02	8.62 ± 0.01
ψ (dex)	0.044 ± 0.01	0.048 ± 0.01

upper-left panels of Figures 5 and 6. Our region of interest for each galaxy⁴ extends approximately out to $0.55 R_{25}$ for M74, and to $0.7 R_{25}$ for M83. So whilst the bulk of the metallicity points lie within the region of interest of each galaxy, providing dense sampling, there are also sufficient points outside it to constrain the metallicity variations over larger scales.

In order to produce maps of κ_d , it was necessary to first have maps of the metallicity distributions of our target galaxies. The first step towards achieving this was modelling their radial metallicity profiles. The spectra metallicity points for M74 and M83, plotted as a function of their deprojected galactocentric radius, r , are shown in Figure 4. As can be seen, there is significant scatter around the radial trends of both galaxies, far in excess of what would be expected if it were driven solely by the uncertainties on the individual metallicity points. Indeed, if one fits a naïve metallicity profile where the only variables are the gradient and the central metallicity, then the majority of datapoints would count as $> 5\sigma$ ‘outliers’ in M83 (and most would count as $> 2\sigma$ outliers for M74). This scatter represents localised variations in metallicity, which are not azimuthally-symmetric – and which therefore cannot be captured by a 1-dimensional model. Such variation becomes apparent when sampling the metallicity within galaxies at such high spatial resolution (Rosales-Ortega et al. 2010; Moustakas et al. 2010). For example, note the localised region of significantly depressed metallicity in the western part⁵ of the disc of M83, visible in the upper-left panel of Figure 6.

We had to take this intrinsic scatter into account when modelling the radial metallicity profiles of our target galaxies; we therefore used a model with 3 parameters: the metallicity gradient m_Z (in dex r_{25}^{-1}), the central metallicity c_Z (in $12 + \log_{10}[\frac{O}{H}]$), and the intrinsic scatter ψ (in dex). We employed a Bayesian Monte Carlo Markov Chain (MCMC) approach to fit this model, the full details of which are given in Appendix A; the resulting parameter estimates, with uncertainties, are listed in Table 2.

It would technically be possible to create metallicity maps of our target galaxies using only these fitted radial metallicity profiles. However, using this simple 1-dimensional approach (ie, where metallicity varies only as a function of r) leads to very large uncertainties on the metallicity value of each pixel in the resulting maps, thanks to the considerable intrinsic scatter values ($\psi = 0.044$ dex for M74, and $\psi = 0.049$ dex for M83). In contrast, most of the individual spectra metallicity datapoints have uncer-

⁴ The region of interest being the area where we map κ_d ; illustrated in Figures 2 and Figure 3, and defined in Section 4.1.

⁵ Centred at approximately: $\alpha = 204.20^\circ$, $\delta = -29.87^\circ$.

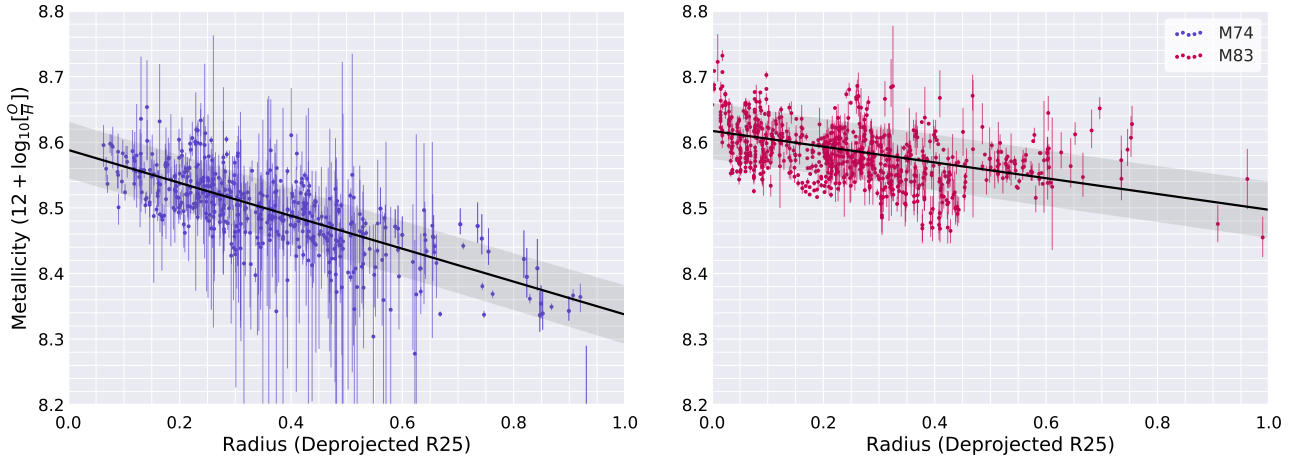


Figure 4. The radial metallicity profiles of M74 (left) and M83 (right). The black lines show the radial metallicity profiles; the shaded grey areas indicate the intrinsic scatter (all based on median posterior values of m_Z , c_Z , and ψ). For ease of viewing, a handful of points are not shown in these plots (being at $12 + \log_{10}[\frac{O}{H}] < 8.2$, and/or radii beyond R_{25}); such points are nonetheless included in all modelling.

tainties much smaller than this, with median uncertainties of 0.010 and 0.025 dex for M74 and M83 respectively (NB, spectra located in close proximity tend to have metallicities that are in good agreement – see the densely-sampled area in Figures 5 and 6). In other words, there are many areas of these galaxies where the metallicity is known to much greater confidence than is reflected by the global radial metallicity gradient – therefore, relying upon the global 1-dimensional model alone would mean ‘throwing away’ that information. As such, we opted to model the metallicity distributions of our target galaxies in 2 dimensions. To achieve this, we employed Gaussian process regression.

3.3.1 Gaussian Process Regression

Gaussian Process Regression (GPR) is a form of probabilistic interpolation, that makes it possible to model a dataset without having to assume any sort of underlying functional form for the model. GPR (and Gaussian process methodology in general) is a commonly-applied tool in the field of machine learning – and in recent years GPR has seen increasing use in astronomy, to tackle problems where stochastic (and therefore impractical to model directly) processes give rise to complex features in data (for instance, capturing the effect of varying detector noise levels in time-domain data). For a full introduction to Gaussian process methodology, including GPR, see Rasmussen & Williams (2006); for an extensive list of works where Gaussian processes have been successfully applied to problems in astronomy, see Section 1 of Angus et al. (2018).

Instead of trying to model the underlying function that gave rise to the observed data, GPR models the covariance between the datapoints. The covariance is modelled using a kernel, which describes how the values of datapoints are correlated with one another, as a function of their separation in the parameter space.

This covariance-modelling approach is well-suited to the problem we face with mapping metallicity within our target galaxies. Spectra located very close together (eg, within

a few arcseconds) will tend to have very similar metallicities, whilst spectra with greater separations (eg, arcminutes apart) will only be weakly correlated with one another (this is readily apparent from visual inspection of Figures 5 and 6).

For the covariance function, we used a Matérn kernel (Stein 1999). The Matérn function is a standard choice for modelling the spatial correlation of 2-dimensional data (Minasny & McBratney 2005; Rasmussen & Williams 2006; Cressie & Wikle 2011) – especially physical data (Schön et al. 2018). In practice, a Matérn kernel is similar to a Gaussian kernel, but has a narrower peak (allowing it to be sensitive to variations over short distances) whilst also having thicker tails (letting it maintain sensitivity to the covariance over large distances). Like a Gaussian, the tails extend to infinity. The Matérn kernel has two hyperparameters: kernel scale, and kernel smoothness (essentially how ‘sharp’ the peak of the kernel is).

Once the covariance has been modelled, it is used in combination with the observed data to trace the underlying distribution. The result is a full posterior Probability Distribution Function (PDF) for the likely value of the underlying function at that location. The uncertainties in each input datapoint are fully considered by GPR. In regions where the input datapoints have large uncertainties, or where datapoints in close proximity disagree with one another, the output PDF will be less well constrained, reflecting the greater uncertainty on the underlying value at that location.

3.3.2 Metallicity Maps Via Gaussian Process Regression

We opted to apply the GPR to the *residuals* between the individual spectra metallicity points and the global radial metallicity profile (ie, Figure 4). By fitting to the residuals, the global radial metallicity profile effectively serves as the prior for the regression. The regression then traces the structure of the local deviations from the global radial metallicity profile. In regions where there are no data points, the GPR

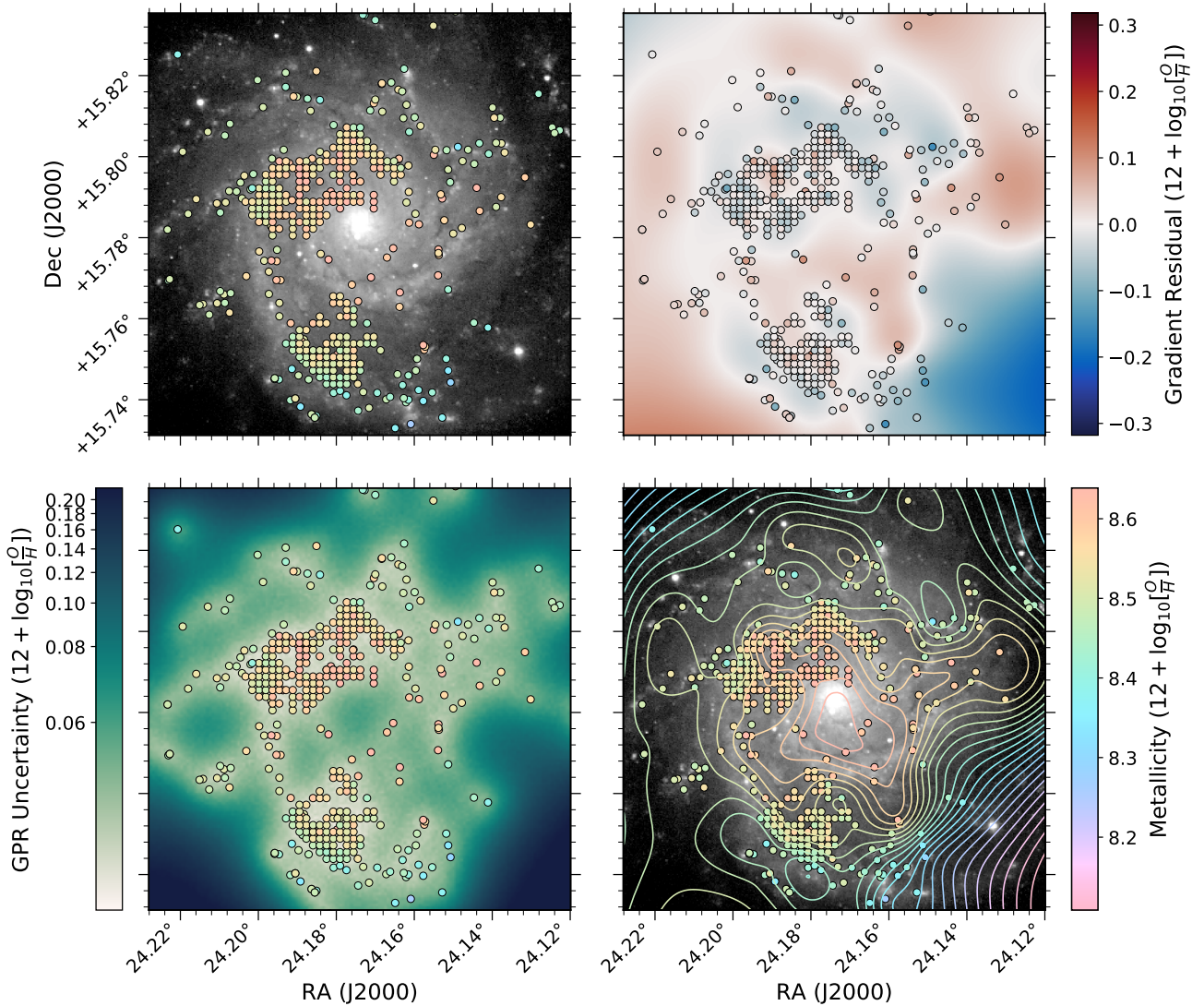


Figure 5. Illustration of our Gaussian Process Regression (GPR) metallicity mapping procedure, for M74. *Upper left:* Markers show the positions of spectra, colour-coded to indicate their metallicity (as per the colour bar at the lower right of the figure), plotted on a *Spitzer* 3.6 μm image. *Upper right:* Points show the residual between the metallicity of each spectra, and the global radial metallicity profile at that position. Red points have a positive residual, blue points have a negative residual. Background image shows the GPR model to these residuals. *Lower left:* Background image shows the uncertainty on the GPR, with positions of spectra plotted on top (again colour coded according to their individual metallicities, as per the colour bar at the lower right of the figure). The regression tends to have much lower uncertainty in area more densely sampled with spectra. *Lower right:* Same as upper left panel, but now with the final GPR metallicity map traced with colour-coded contours. This final metallicity map was produced by adding the GPR residual model shown, in the upper right panel, to the global radial metallicity profile. The colour scale used to indicate metallicity is red-to-red circular (therefore preserving sequentiality for all kinds of colour blindness) and approximately isoluminant (therefore reverting to a near-constant shade when displayed in greyscale).

therefore tends to revert to the metallicity implied by the global radial profile.

This process is illustrated in the upper-right panels of Figures 5 and 6 for M74 and M83 respectively. The circular points mark the positions of the individual spectra metallicities, colour-coded to show the residual of each (the median absolute residual is 0.026 dex for both galaxies). The coloured background shows the Gaussian process regression to these residuals, similarly colour-coded. We used

`GaussianProcessRegressor`, the GPR implementation of the Scikit-Learn machine learning package for Python (Pedregosa et al. 2011). The hyperprior for the kernel scale was flat, but limited to a range of 0.05–0.5 D_{25} , to prevent the modelled regression being either featurelessly smooth, or unrealistically granular. The kernel smoothness hyperprior was set to 1.5, which is a standard choice due to being computationally efficient, differentiable, and often found to be effective in practice (Rasmussen & Williams 2006; Gatti 2015).

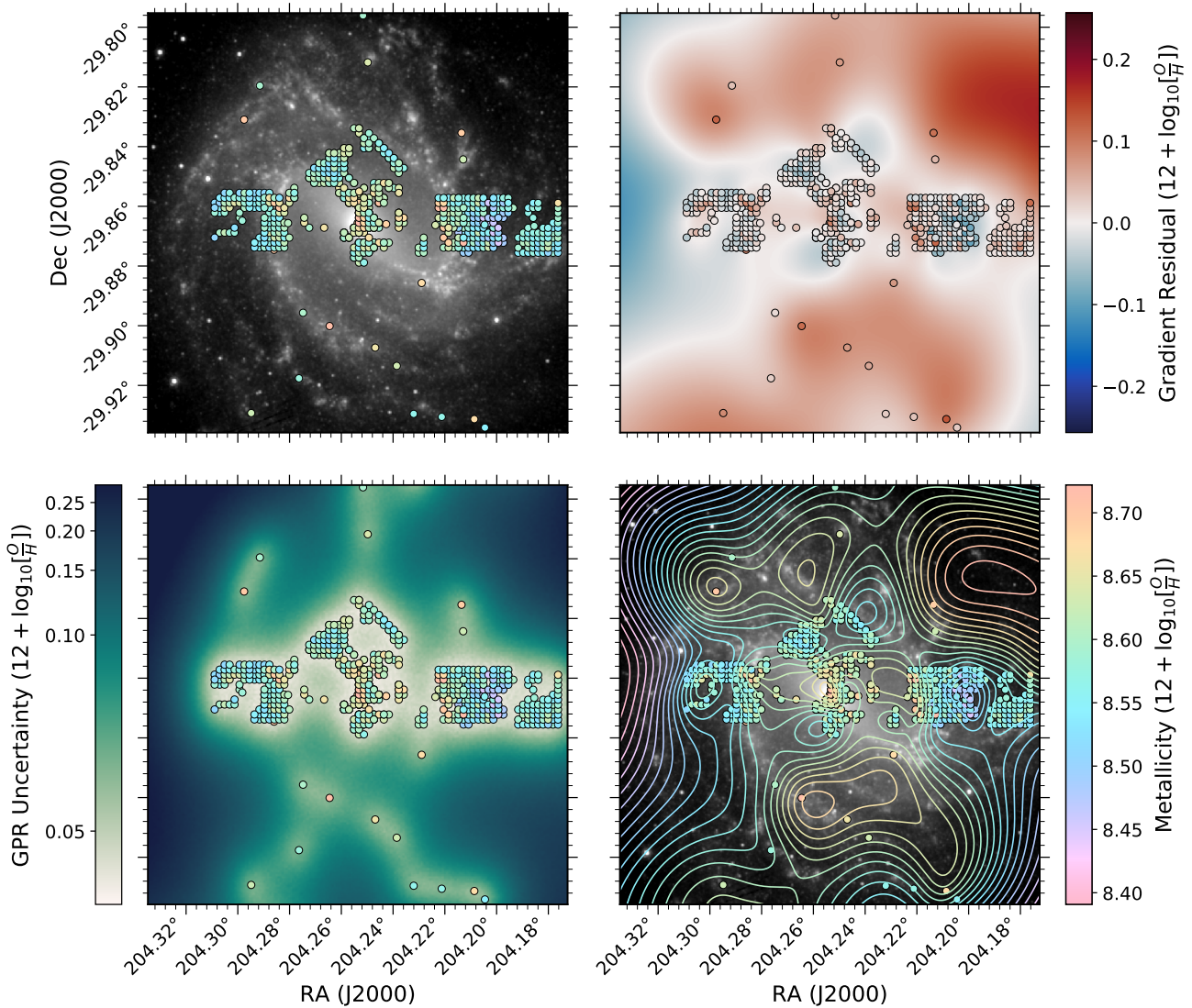


Figure 6. Metallicity mapping for M83. Description as per Figure 5. Localised variations in metallicity are as prominent as the global gradient, as expected given Figure 4. The high-metallicity (and high-uncertainty) region extrapolated by the GPR to the northwest of M83 is driven by the fact that the closest spectra to this area have metallicities above what would be predicted from the global gradient.

The final metallicity map for each galaxy was produced by adding the residual distribution traced by the GPR to the global radial metallicity profile, for each pixel. The resulting metallicity maps are plotted as contours in the lower-right panels of Figures 5 and 6, for M74 and M83 respectively. Visual inspection indicates that the GPR does a good job of tracing the metallicity distribution as sampled by the spectra metallicity points (ie, the contours consistently have the same levels as the points they pass through).

Our full procedure for calculating the uncertainty on the GPR metallicity in each pixel is presented in Appendix C. The resulting metallicity uncertainty maps are shown in the lower-left panels of Figures 5 and 6.

We validated the reliability of the metallicities predicted by GPR by performing a jackknife cross-validation analysis, which is described in detail in Appendix B. This analysis

found that the predicted values exhibit no significant bias, and the associated uncertainties are reliable.

There are areas in both galaxies where the datapoints suggest a steadily-increasing residual in a certain direction; the GPR then extrapolates that this increase continues for some distance (defined by the modelled kernel scale) into regions where there are no datapoints. For instance, in the south-western part of M74, the datapoints suggest that the metallicity gradient is steeper than for the rest of the galaxy (ie, a trend of increasingly negative residuals) – the GPR extrapolates that this increased steepness will continue for a certain distance into an area where there are no metallicity points. A similar situation occurs in the north-west portion of M83 (but instead with a positive residual). Naturally, extrapolations such as these are highly uncertain; but this is quantified by the uncertainty on the regression at these loca-

tions. This is illustrated in the lower-left panels of Figures 5 and 6, which show the uncertainty for each pixel’s predicted metallicity.

Utilising GPR provides a marked reduction in the uncertainty of our metallicity maps, relative to using the global radial metallicity profiles alone. If we were to use that simple global approach, every pixel in our metallicity map for M74 would have an uncertainty at least as large as the intrinsic scatter of 0.044 dex (Table 2). In contrast, with our GPR metallicity map of M74, 91% of the pixels within the region of interest⁴ have uncertainties < 0.044 dex; the median GPR uncertainty within this region is only 0.016 dex. Similarly, whereas the intrinsic scatter on the global radial profile of M83 is 0.048 dex, the median error on the GPR metallicity map is only 0.037 dex within the region of interest; the GPR uncertainty is less than the global intrinsic scatter for 66% of the pixels within this region.

There exist ‘direct’ electron temperature metallicity measurements for M74, produced by the CHemical Abundances Of Spirals (CHAOS; Berg et al. 2015). Electron temperature metallicities are at reduced risk of systematic errors, compared to strong-line values like those provided by De Vis et al. (2019). However, the CHAOS data for M74 only consists of 45 measurements. Whilst we trialled producing metallicity maps with this data, the sparse sampling meant that the uncertainty on the metallicity at any given point was extremely large. Maps of κ_d produced with these metallicity maps (as per the procedure described in Section 4) were so dominated by the resulting noise that they were not informative.

3.4 Atomic & Molecular Gas Data

Atomic and molecular gas data for a sample of extended, face-on spiral galaxies in DustPedia – including those studied in this work – is presented in Casasola et al. (2017). For both of our target galaxies, we followed Casasola et al. (2017) and use HI data from The HI Nearby Galaxy Survey (THINGS; Walter et al. 2008), which conducted 21 cm observations of 34 nearby galaxies with the Very Large Array, at 6–16'' resolution. We retrieved the naturally-weighted moment 0 maps for M74 and M83 from the THINGS website⁶. The HI maps for both galaxies are shown in the 3rd panels of Figures 2 and 3.

To obtain CO observations for M74 we again followed Casasola et al. (2017), and used data from the HERA CO Line Extragalactic Survey (HERACLES; Leroy et al. 2009), which performed CO(2-1) observations of 18 nearby galaxies using the IRAM 30 m telescope, at 13'' resolution. We retrieved the moment 0 maps, as associated uncertainty maps, from IRAM’s official HERACLES data repository⁷. The CO(2-1) map for M74 is shown in the 4th panel of Figure 2.

Although M74 has been observed in CO(1-0) by various authors (Young et al. 1995; Regan et al. 2001), these observations are all lacking in either resolution, sensitivity, and/or coverage, in comparison to the HERACLES data.

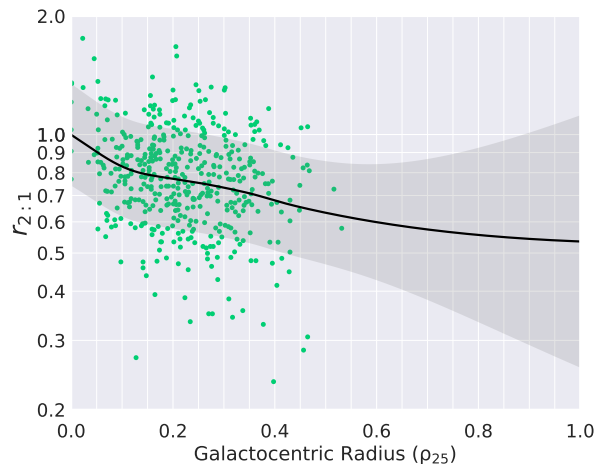


Figure 7. $r_{2:1}$ values from Figure 34 (lower-right panel) of Leroy et al. (2009), plotted against galactocentric radius in terms of R_{25} . The black line shows our Gaussian process regression to this data, with the grey shaded area indicating the 1σ uncertainty.

We therefore found it preferable to use the CO(2-1) data of HERACLES, despite the fact this requires applying a line ratio, $r_{2:1} = I_{\text{CO}(2-1)}/I_{\text{CO}(1-0)}$, in order to find $I_{\text{CO}(1-0)}$, and hence calculate H_2 mass as per Equation 6.

In nearby late-type galaxies, $r_{2:1}$ has an average value of ~ 0.7 (Leroy et al. 2013; Casasola et al. 2015; Saintonge et al. 2017). However, it is also known that $r_{2:1}$ varies significantly with galactocentric radius (Casoli et al. 1991; Sawada et al. 2001; Leroy et al. 2009). As such, accurately inferring the CO(1-0) distribution in M74 using the HERACLES CO(2-1) map required a radially-dependent $r_{2:1}$. To produce this, we used the data presented in Figure 34 (lower-right panel) of Leroy et al. (2009), where they compare the HERACLES $I_{\text{CO}(2-1)}$ maps to literature $I_{\text{CO}(1-0)}$ maps of the same galaxies produced by several other telescopes (with appropriate corrections applied to account for differences in spatial and velocity resolution). This yielded ≈ 450 directly-measured $r_{2:1}$ values, spanning radii from 0–0.55 R_{25} , for 9 of the HERACLES galaxies. Leroy et al. (2009) simply binned these points to trace the radial variation in $r_{2:1}$; however, we chose to take a fully probabilistic approach, and use GPR to infer the underlying radial trend in $r_{2:1}$. In Figure 7, we plot all of the $r_{2:1}$ points from Figure 34 (lower-right panel) of Leroy et al. (2009). We applied a GPR to this data, using a Matérn covariance kernel. Because $r_{2:1}$ is a ratio, we constructed the regression so that the output uncertainties are symmetric in logarithmic space; otherwise, output uncertainties symmetric in linear space would extend to unphysical values of $r_{2:1} < 0$ at larger radii. The resulting regression is shown in black in Figure 7. It is in excellent agreement with the radial trend that Leroy et al. (2009) traced by binning the data, with $r_{2:1}$ elevated to ~ 1 in the galaxies’ centres, falling to 0.7–0.8 over the rest of the sampled region – but our approach has the added benefit over binning of providing well-constrained uncertainties on $r_{2:1}$ values produced using the regression. The uncertainty associated with the regression is a factor of ≈ 1.3 over the $0 < R/R_{25} < 0.55$ range in radius sampled by the HERACLES measurements, reflecting the intrinsic scatter present in the datapoints; beyond this,

⁶ <https://www.mpia.de/THINGS/Overview.html>

⁷ <https://www.iram-institute.org/EN/content-page-242-7-158-240-242-0.html>

the uncertainty steadily increases, reaching a factor of ≈ 2 at $R = R_{25}$. Given the uncertainty on α_{CO} , this does not represent a large addition to the total uncertainty on the molecular gas masses we calculated.

M83 was not observed by HERACLES. So we instead used the CO(1-0) observations presented in [Lundgren et al. \(2004\)](#), which were made using the Swedish–ESO Submillimetre Telescope (SEST) at a resolution of $42''$, to a uniform depth of 74 mK (T_{mb}). The CO(1-0) map for M83 is shown in the far-right panel of Figure 3.

We determined α_{CO} pixel-by-pixel using our metallicity maps according to Equation 7, and thereby produced H_2 maps of our target galaxies. The total H_2 masses contained in these maps are the H_2 masses listed in Table 1.

4 APPLICATION

4.1 Data Preparation

We background-subtracted all continuum maps following the procedure described in [Clark et al. \(2018\)](#), using the background annuli they specify for our target galaxies.

All data (continuum observations, gas observations, and metallicity maps) were smoothed to the resolution of the most poorly-resolved observations for each galaxy. This was done by convolving each image with an Airy disc kernel of Full-Width Half-Maximum (FWHM) given by $\theta_{\text{kernel}} = (\theta_{\text{worst}}^2 - \theta_{\text{data}}^2)^{\frac{1}{2}}$. We therefore convolve all of our M74 data to the $36''$ resolution of the *Herschel*-SPIRE 500 μm observations. Likewise, we convolved all of our M83 data to the $42''$ resolution of the SEST HI observations.

We reprojected all of our data to a common pixel grid for each galaxy, on an east–north gnomonic tan projection. We wished to preserve angular resolution, ensuring that our data remain Nyquist sampled, to maximise our ability to identify any spatial features or trends in our final κ_d maps. We therefore used projections with 3 pixels per convolved FWHM. This corresponds to $12''$ pixels for M74, and $14''$ pixels for M83.

For each galaxy, we defined a region of interest, within which all required data is of sufficient quality to effectively map κ_d . We defined this as being the region within which all pixels in the smoothed & reprojected versions of the HI map, CO map, and 22–500 μm continuum maps, have $\text{SNR} > 2$ (as defined by comparison to their respective uncertainty maps). For both M74 and M83, the data with the limiting sensitivity are the CO observations. The borders of our regions of interest for both galaxies are shown in the far-right panels of Figures 2 and 3.

4.2 SED Fitting

As described in Section 2, the dust-to-metals method lets us establish dust masses *a priori*; then, by comparing this *a priori* dust mass to observed FIR–submm dust emission, we can calibrate the value of κ_d . This necessitates having a model that describes that FIR–submm dust emission. We wished to minimise the scope for potentially-incorrect model assumptions to corrupt our resulting κ_d values. We therefore modelled the dust emission with the simplest model that is able to fit FIR–submm fluxes – a one-component

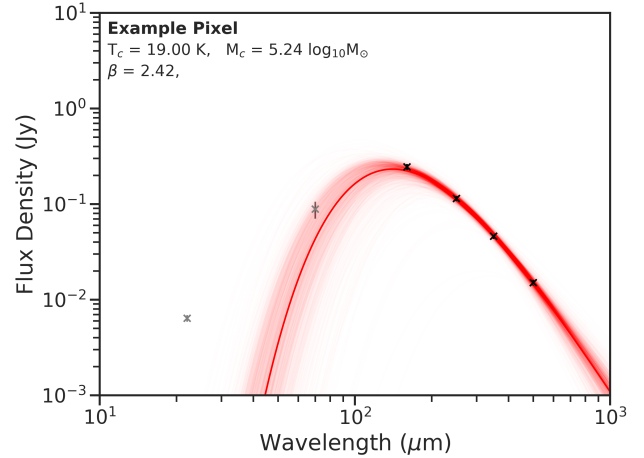


Figure 8. The posterior SED modelled by our SED fitting for an example pixel in M74 (specifically, at $\alpha = 24.1820^\circ$, $\delta = 15.7755^\circ$). The black crosses show standard fluxes, whilst the grey crosses are fluxes that serve as upper limits; error bars are drawn for both. The pale red translucent lines show the SEDs corresponding to 500 samples from the posterior distribution. The solid red line shows the data space median posterior SED (being the posterior sample for which half of all other samples are brighter, and half fainter, averaged over the wavelength range for which data is present), and the text in the figure give its parameters. The corresponding posterior parameter distributions are shown in Figure 9.

MBB (ie, Equation 1, with $n = 1$). A one-component MBB model has been shown by many authors to break down in various circumstances (eg: [Jones 2013](#); [Clark et al. 2015](#); [Chastenet et al. 2017](#); [Lamperti et al. submitted](#)). However, these primarily concern either submillimetre excess in low-metallicity and/or low-density environments (which are not present in the regions of interest within our target galaxies), the emission from hotter dust components at short wavelengths (which we do not attempt to model; see below), or features only discernable in spectroscopy (which we are not employing). In ‘normal’ galaxies, a one-component MBB can be expected to fit FIR–submm fluxes successfully ([Nersesian et al. 2019](#)).

Note that, as a test, we also repeated the entire SED fitting process described in this section with a two-component MBB model (ie, Equation 1, with $n = 2$, giving dust components at two temperatures). However, when comparing the χ^2 values of both sets of fits, we found that adopting the two-component MBB approach adds little benefit to the quality of the fits. The median reduced χ^2 values (of all posterior samples, from all pixels) for the one-component MBB fits were 0.61 for M74 and 0.94 for M83 – compared to 0.59 and 0.65 respectively for the two-component fits. This indicates that the two-component MBB fits offer minimal improvement over the one-component fits (and, indeed, may be straying into the realm of over-fitting). Given our desire to employ the simplest applicable model, we therefore opt to proceed with the one-component MBB approach for this work. Nonetheless, in Appendix G, we verify that the choice of one- or two-component SED fitting does not result in considerable changes to our overall results.

By performing our SED fitting pixel-by-pixel, we are

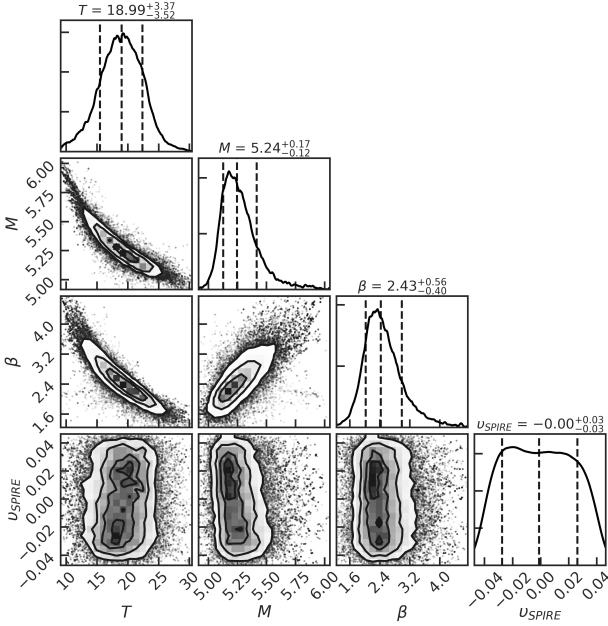


Figure 9. Corner plot showing the covariances of the posterior distributions of the free parameters modelled in our SED fitting, for an example pixel in M74 (specifically, at $\alpha = 24.1820^\circ$, $\delta = 15.7755^\circ$). The two-parameter distributions have contours indicating the regions containing 68.3%, 95.5%, 99.7%, and 99.9% of the posterior samples; probability density is indicated as a shaded density histogram within the contoured region, whilst outside of the contoured region the samples are plotted as individual points. The individual parameter distributions, plotted at the top of each column as KDEs, are annotated with the median values, along with the boundaries of the 68.3% credible interval as \pm values (with masses given in units of $\log_{10} M_\odot$). The corresponding posterior SEDs, plotted in data space, are shown in Figure 8.

reducing the degree to which there will be contributions from multiple dust components at different temperatures. Nonetheless, there will inevitably be some degree of line-of-sight mixing of dust populations. This risk will be greatest in the densest regions, where fainter emission from colder, but potentially more massive, dust components can be dominated by brighter emission from warmer, but less massive, components heated by star-formation (Malinen et al. 2011; Juvela & Ysard 2012). If this does occur, then the resulting κ_d values will, in effect, factor in the mass of any cold dust component too faint to affect the SED (assuming the *a priori* dust masses calculated by the dust-to-metals method are accurate). In this scenario, the κ_d values we calculate may not be valid if applied to observations with good enough spatial resolution that line-of-sight mixing becomes negligible.

Although we use Equation 1 to model SEDs, we assign an arbitrary value of κ_λ during the fitting process (as, of course, the SED fitting is being performed in order to allow us to find a value of κ_λ using the results). This means that the ‘mass’ parameter yielded by our SED fitting merely serves as a normalisation term for the SED amplitude. This is not a problem, as the only output values actually required is the temperature of the dust, and its flux at the reference wavelength; these are needed in Equation 3 to calculate values of κ_d .

We also incorporate a correlated photometric error pa-

rameter, v_{SPIRE} , into our SED-fitting. The photometric calibration uncertainty of the *Herschel*-SPIRE instrument contains a systematic error component that is correlated between bands (Griffin et al. 2010; Bendo et al. 2013; Griffin et al. 2013). This arises from the fact that *Herschel*-SPIRE was calibrated using observations of Neptune; however, the reference model of Neptune’s emission has a $\pm 4\%$ uncertainty. We account for this by parameterising the correlated *Herschel*-SPIRE error as v_{SPIRE} . The $\pm 4\%$ scale of v_{SPIRE} accounts for the majority of the combined 5.5% calibration uncertainty of *Herschel*-SPIRE⁸. As such, for high-SNR sources (such as bright pixels within our target galaxies), where the photometric noise is minimal, the correlated calibration error can actually dominate the entire uncertainty budget. Moreover, the $\pm 4\%$ error on v_{SPIRE} does not follow the Gaussian or Student’s *t* distribution typically assumed for photometric uncertainties – rather, it is essentially flat, with the true value of the correlated systematic error almost certainly lying somewhere within the $\pm 4\%$ range (Bendo et al. 2013; A. Papageorgiou, *priv. comm.*; C. North, *priv. comm.*). Explicitly handling v_{SPIRE} as a nuisance parameter allows us to properly account for this with a matching prior. Gordon et al. (2014) highlight the significant differences that can be found in dust SED fitting when the correlated photometric uncertainties are considered, compared to when they are not.

The *Herschel*-PACS instrument also has a systematic calibration error, of $\pm 5\%$, arising from uncertainty on the emission models of its calibrator sources, a set of 5 late type giant stars (Balog et al. 2014). However, the error budget on the emission models is dominated by the $\pm 3\%$ uncertainty on the line features in the atmospheres of the calibrator stars (see Table 2 of Decin & Eriksson 2007), which are different in each band, and hence not correlated. Only the uncertainty on the continuum component of the emission model, of $\pm 1\text{--}2\%$, will be correlated between bands. Given the small scale of this correlated error component, and given that systematic error makes up a smaller fraction of the total *Herschel*-PACS calibration uncertainty than it does for *Herschel*-SPIRE, and given that the greater instrumental noise for *Herschel*-PACS means that calibration uncertainty makes up a small fraction of the total photometric uncertainty budget than it does for *Herschel*-SPIRE, we opt to not model the correlated uncertainty for *Herschel*-PACS as we do with v_{SPIRE} .

Our one-component MBB SED model therefore has 4 variables: the dust temperature, T_d ; the dust ‘mass’ normalisation, $M_d^{(\text{norm})}$; the emissivity slope, β ; and the correlated photometric error in the *Herschel*-SPIRE bands, v_{SPIRE} .

The resulting likelihood function, for a set of fluxes S (in Jy), observed at a set of wavelengths λ (in m), with a corresponding set of uncertainties σ (in Jy), for a set of size n_λ , takes the form:

$$\mathcal{L}(S|\lambda, \sigma, T_d, M_d^{(\text{norm})}, \beta, v_{\text{SPIRE}}) = \prod_i^{n_\lambda} (t(d, S_{d_i}, \sigma_i) + S_{d_i} v_{\text{SPIRE}}) \quad (8)$$

⁸ SPIRE Instrument & Calibration Wiki: <https://herschel.esac.esa.int/twiki/bin/view/Public/SpireCalibrationWeb>

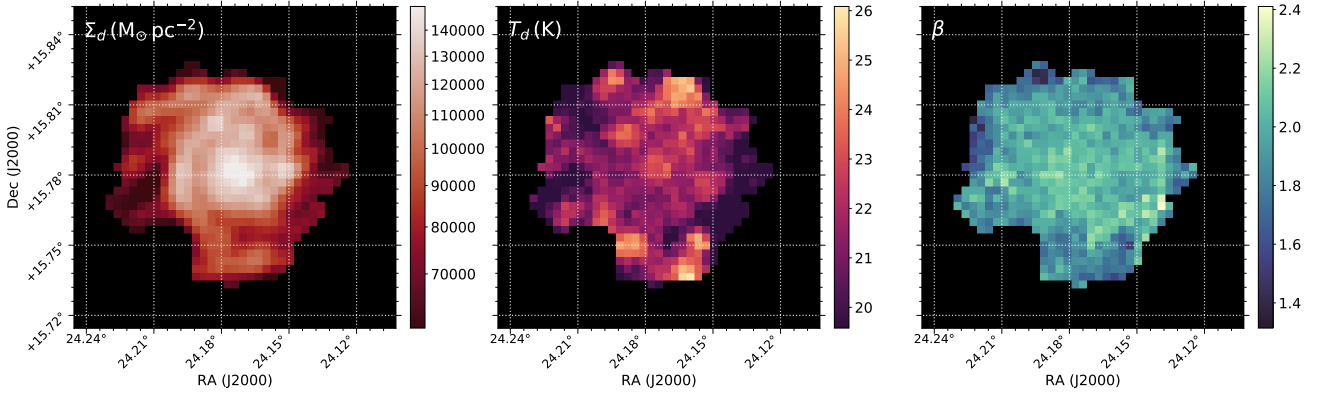


Figure 10. Maps showing the results of our SED fitting of M74. *Left:* Map of dust mass surface density (Σ_d , in $M_\odot \text{pc}^{-2}$). *Centre:* Map of dust temperature (T_d , in K). *Right:* Map of dust emissivity spectral index (β).

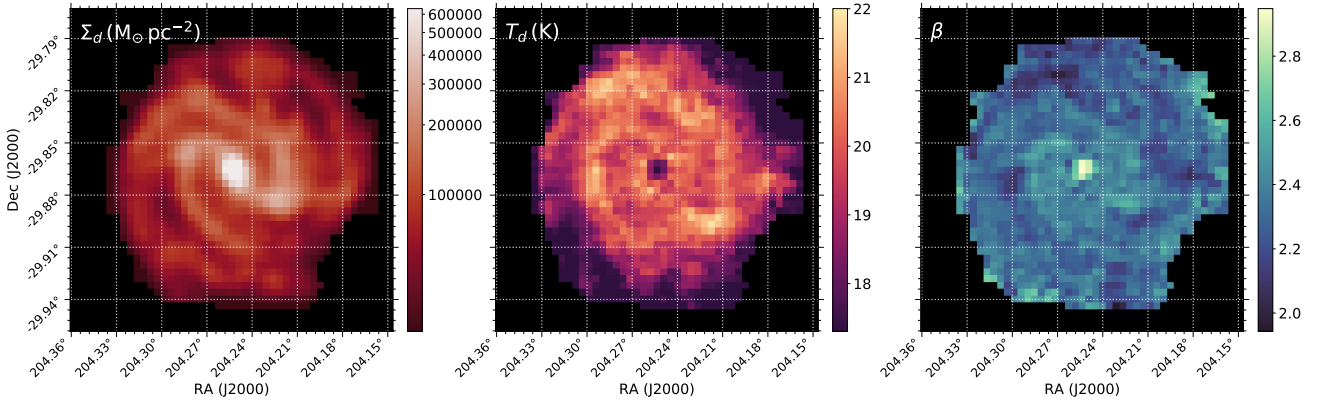


Figure 11. Maps showing the results of our SED fitting of M83. Description as per Figure 10.

where, for the i^{th} wavelength in the set, S_{d_i} is the flux arising from dust emission given the SED model parameters, and σ_i is the corresponding uncertainty; $t(d, S_{d_i}, \sigma_i)$ is a d^{th} -order Student t distribution⁹, centred at a mode of S_{d_i} , with a width of σ_i . The expected dust emission S_{d_i} is given by:

$$S_{d_i} = \frac{1}{D^2} \kappa_0 \left(\frac{\lambda_0}{\lambda_i} \right)^\beta M_d^{(\text{norm})} B(\lambda_i, T_d) \quad (9)$$

We treat photometric uncertainties as being described by a 1st-order (ie, one degree of freedom) Student t distribution. The Student t distribution has more weight in the tails than a Gaussian distribution, allowing it to better account for outliers. This makes the Student t distribution a standard choice for Bayesian SED fitting (da Cunha et al. 2008; Kelly et al. 2012; Galliano 2018).

For the photometric uncertainty in each pixel, we used the values provided by the uncertainty maps, added in quadrature to the calibration uncertainty of each band: 5.6%

for WISE 22 μm ¹⁰, 7% for *Herschel*-PACS 70–160 μm ¹¹, and 2.3%¹² for *Herschel*-SPIRE 250–500 μm ⁸. Both of our target galaxies lie in regions with negligible contamination from Galactic cirrus. The WISE and *Herschel*-PACS backgrounds are dominated by instrumental noise, whilst the *Herschel*-SPIRE background has a significant contribution from the confused extragalactic background. Therefore, for the *Herschel*-SPIRE data, we also add in quadrature the contribution of confusion noise; for this we use the values given in Smith et al. (2017), of 0.282, 0.211, 0.105 MJy sr^{-1} at 250, 350, and 500 μm respectively, derived from the *Herschel*-ATLAS fields (although the instrumental noise level still dominates over this in all of our *Herschel*-SPIRE data).

We treat fluxes at wavelengths $< 100 \mu\text{m}$ as upper limits, as emission in this regime will include contributions from hot dust and stochastically heated small grains (Boulanger & Perault 1988; Desert et al. 1990; Jones et al. 2013) that will not be accounted for by our MBB model. Therefore at

⁹ Standardised to allow modes and widths other than zero, as per the SciPy (Jones et al. 2001) implementation: <https://docs.scipy.org/doc/scipy/reference/generated/scipy.stats.t.html>

¹⁰ WISE All-Sky Release Explanatory Supplement (Cutri et al. 2012): https://wise2.ipac.caltech.edu/docs/release/allsky/expsup/sec4_4h.html

¹¹ PACS Instrument & Calibration Wiki: <https://herschel.esac.esa.int/twiki/bin/view/Public/PacsCalibrationWeb>

¹² 2.3% being the non-correlated component of the *Herschel*-SPIRE calibration uncertainty, separate from v_{SPIRE} .

these wavelengths, any proposed model flux that falls below the observed flux will be deemed as likely as the observed flux itself (ie, no proposed model will be penalised for under-predicting the flux in these bands). Only for proposed model fluxes greater than the observed flux will the likelihood decrease according to the Student t distribution, as per usual.

We sample the posterior probability distribution of the SED model parameters in each pixel using the emcee (Foreman-Mackey et al. 2013) MCMC package for Python. We perform 750 steps with 500 chains (‘walkers’); the first 500 steps from each chain were discarded as burn-in, and non-convergence was checked for using the Geweke diagnostic¹³ (Geweke 1992). Our priors are detailed in Appendix D.

Our SED fitting routine incorporates colour-corrections to account for the effects of the instrumental filter response functions and beam areas^{14,15,16,17}. An example posterior SED, along with the corresponding parameter distributions, are shown in Figures 8 and 9.

Figures 10 and 11 show maps of the median values of dust mass surface density, temperature, and β values for each pixel. We assume that the low temperatures and large β values found in the centre of M 83 are non-physical, and instead are due to non-thermal emission from the nuclear starburst affecting the SED-fitting. This is limited to a beam-sized area, consisting of 9 pixels - we therefore exclude these pixels from analysis in later sections, where noted.

Unsurprisingly, the maps of dust mass surface density closely match the morphology of the dust emission (see Figures 2 and 3). The temperature map for M 74 is ‘blotchy’, with warmer dust being located around areas of particularly active star formation (compare to the regions of bright MIR emission in Figure 2 in the northern and southern parts of the disc). The temperature map for M 83 more visibly traces the overall spiral structure; in particular, elevated temperatures are found on the exterior edges of the spiral arms. The β maps for both galaxies show correlations with the dust mass surface density; in M 74 this manifests as a broad global trend of beta decreasing with radius, whilst in M 83 beta again more obviously traces the spiral structure.

There is a well-known anticorrelation between temperature and β when performing MBB SED fits (Shetty et al. 2009; Kelly et al. 2012; Galliano et al. 2018). This is clearly in evidence in Figure 9. However, as demonstrated by Smith et al. (2012), this does not introduce *systematic* errors into the results of such fits. And given this lack of systematic bias, the anticorrelation will not introduce spurious trends into resolved SED fits – because fits separated by more than one beam-width will be independent, and will be no more

likely to be biased one way than the other. Combined with the fact that we sample the full posterior in our SED fits, and propagate this into the final calculation of our κ_d maps (see Section 5), we do not believe that the temperature- β anticorrelation will compromise the validity of our final results.

Our SED fitting code has been made freely available online as a Python 3 package¹⁸.

5 RESULTS

We now have the atomic gas, molecular gas, metallicity, and dust emission data necessary for every pixel in order to create maps of κ_d for our target galaxies.

For every pixel within the region of interest for each galaxy, we produced a full posterior probability distribution for κ_d . We did this by drawing random samples from the posterior distributions provided by our SED and metallicity maps (which are independent of one another), and inputting them into Equation 3 (with number of MBB SED components $i = 1$, as per Section 4.2). For all other input values (S_{HI} , I_{CO} , α_{CO} , $\alpha_{\text{CO}_{\text{MW}}}$, y_{CO} , $r_{2:1}$, δ_{O} , $f_{\text{Z}\odot}$, $[12 + \log_{10} \frac{\text{O}}{\text{H}}]_{\odot}$, f_{He_p} , $[\frac{\Delta f_{\text{He}}}{\Delta f_{\text{Z}}}]$, and ϵ_d) we drew random samples from the Gaussian distributions described by their adopted values and associated uncertainties (effectively assuming flat priors, so that these can be treated as posterior probabilities).

We calculated κ_d for a reference wavelength of 500 μm , as this is the longest wavelength for which we have data, and therefore the wavelength where emission is least sensitive to dust temperature; this minimises the degree to which uncertainty in temperature is propagated to κ_d . Our resulting maps of κ_{500} , produced by taking the posterior median in each pixel, are shown in Figures 12, and 13. These maps contain 585 and 1269 pixels for M 74 and M 83 respectively. Throughout the rest of this work, quoted κ_{500} values are pixel medians. The overall median across M 74 is $\kappa_{500} = 0.15 \text{ m}^2 \text{ kg}^{-1}$, whilst the overall median across M 83 is $\kappa_{500} = 0.26 \text{ m}^2 \text{ kg}^{-1}$.

The uncertainties on these κ_{500} values (defined by the 68.3% quantile in absolute deviation away from the median along the posterior distribution) span the range 0.21–0.28 dex, with a mean uncertainty of 0.25 dex for both galaxies. Note that a large degree of this uncertainty is shared across all pixels, due to the contributions of systematics (such as the uncertainties on ϵ_d , $\alpha_{\text{CO}_{\text{MW}}}$, etc), which is why the 0.25 dex average uncertainty is large relative to the scatter in κ_{500} values. We determined the contribution of the systematic components to the overall uncertainty via a Monte Carlo simulation, in which κ_{500} values were generated according to Equation 3, but where only input parameters with systematic uncertainties were allowed to vary. The scatter on the output dummy values of κ_{500} was taken to represent the total systematic uncertainty. On average, we found that the systematic components contribute 0.20 dex to the uncertainty. Taking the quadrature difference between this and our average total uncertainty gives an average statistical uncertainty of 0.15 dex in κ_{500} .

The values in our κ_{500} maps are not fully independent,

¹³ Comparing the means of the last 90–100% quantile of the combined chains to the 50–60% quantile.

¹⁴ WISE colour corrections from Wright et al. (2010).

¹⁵ *Spitzer*-MIPS colour corrections from the MIPS Instrument Handbook, version 3 (Colbert 2011): https://irsa.ipac.caltech.edu/data/SPITZER/docs/mips/mipsinstrumenthandbook/51/#_Toc288032329

¹⁶ *Herschel*-PACS colour corrections from the PACS Handbook, version 4.0.1 (Exter et al. 2019): <https://www.cosmos.esa.int/documents/12133/996891/PACS+Explanatory+Supplement>

¹⁷ *Herschel*-SPIRE colour corrections from the SPIRE Handbook, version 3.1 (Valtchanov et al. 2017): https://herschel.esac.esa.int/Docs/SPIRE/spire_handbook.pdf

¹⁸ <https://github.com/Stargazer82301/ChrisFit>

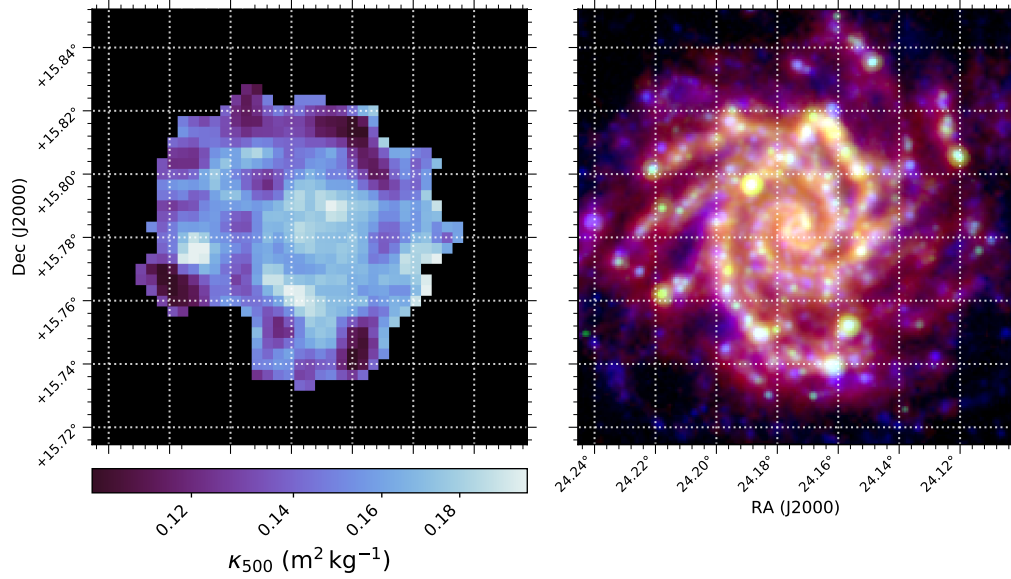


Figure 12. *Left:* Map of κ_{500} within M74. *Right:* UV–NIR–FIR three-colour image of M74, shown for comparison.

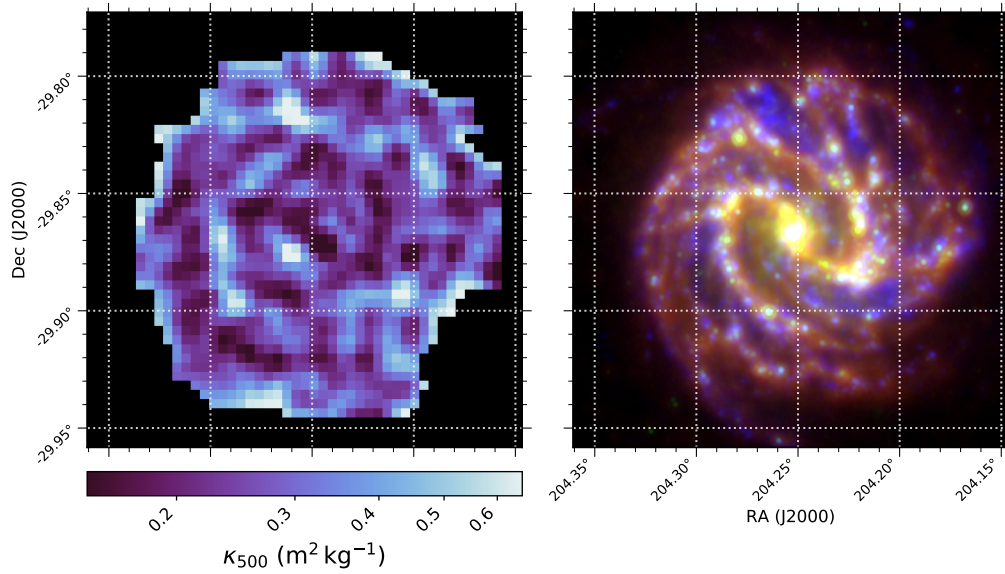


Figure 13. *Left:* Map of κ_{500} within M83. *Right:* UV–NIR–FIR three-colour image of M83, shown for comparison.

as they have a pixel width of 3 pixels per FWHM; this will render adjacent pixels correlated. Therefore we also produced a version of the κ_{500} maps with pixels large enough to be independent (ie, 1 pixel per FWHM). These maps contained 65 and 141 independent κ_{500} measurements for M74 and M83 respectively. When performing statistical analyses throughout the rest of this work, we used these maps in order to ensure the validity of the results. However, the use of larger pixels for these maps does involve throwing away spatial information. We therefore present the standard,

Nyquist-sampled maps in Figures 12, 13, and elsewhere, in order to display all of the spatial information our data is able to resolve. Similarly, individual points plotted in Figure 14 and elsewhere represent the pixels from the Nyquist-sampled maps, although the trend lines shown on these plots are derived from the independent-pixel data.

In order to calculate a robust estimate of the underlying range of κ_{500} values, we performed a non-parametric bootstrap resampling of the pixel medians. This non-parametric bootstrap approach will account for the statistical scatter,

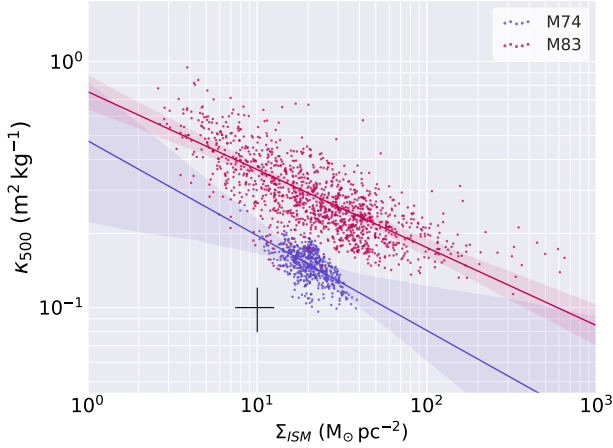


Figure 14. Plot of κ_{500} against ISM surface density (as traced by molecular and atomic gas) for M74 and M83. The best fit power laws for both galaxies are shown, with shaded regions indicating the 68.3% credible intervals. The black cross indicates the median 1σ error bars (indicating only the statistical uncertainty, omitting systematic uncertainties, as discussed in the text).

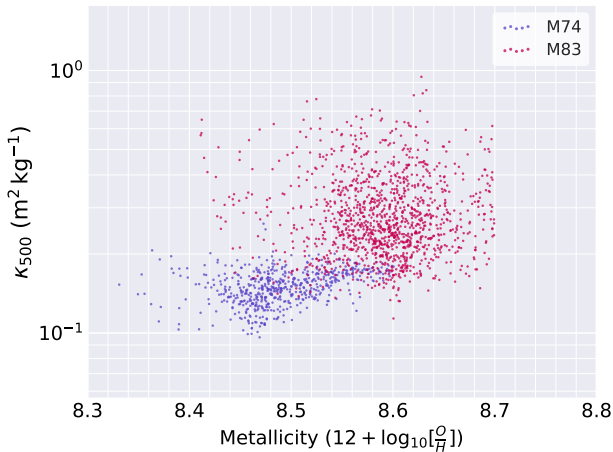


Figure 15. Plot of κ_{500} against gas-phase metallicity, expressed in terms of oxygen abundance, for M74 and M83.

and not encompass the systematics. This gives a median underlying range for $0.11\text{--}0.25\text{ m}^2\text{ kg}^{-1}$ for M74 (a factor of 2.3 variation), and $0.15\text{--}0.80\text{ m}^2\text{ kg}^{-1}$ for M83 (a factor of 5.3 variation).

There is a strong relationship between κ_{500} and Σ_{ISM} (the ISM mass surface density, where $\Sigma_{ISM} = \Sigma_{H_1} + \Sigma_{H_2} + \Sigma_d$) as shown in Figure 14. Both galaxies exhibit this relation, but are curiously separated, with the relation for M74 lying ~ 0.3 dex beneath that of M83. We are able to trace this behaviour over a much larger range of Σ_{ISM} for M83 than for M74 – the densest regions of M83 are much denser than those of M74, whilst the deeper CO data for M83 allows us to probe to regions of lower density. This neatly accounts for the fact that we find a narrower range of κ_{500} values for M74 than M83 – whilst we probe a 1.7 dex range in density in the latter, we only probe 0.7 dex in the former. We estimated κ_{500} vs Σ_{ISM} power laws for each

galaxy by performing a Theil-Sen regression (Theil 1992) to each set of posterior samples in our κ_{500} and Σ_{ISM} maps (specifically, the independent-pixel version of the maps, as discussed above). The resulting power law slopes for both galaxies are in good agreement, with their indices being $-0.35^{+0.26}_{-0.21}$ for M74 and $-0.36^{+0.04}_{-0.05}$ for M83. As discussed in Section 6.3, this behaviour is in contradiction to positive correlation between κ_d and ISM density predicted by standard dust models. The median statistical uncertainty on pixel values of Σ_{ISM} is 0.13 dex; given the similarly-small 0.15 dex average statistical uncertainty on κ_{500} , we can be confident that the trend in Figure 14, which spans 1.7 dex for M83, isn't merely a spurious noise induced correlation. The rank correlation coefficient of the relationship is $\tau = -0.36$ for M74, and $\tau = -0.57$ for M83 (from a Kendall tau rank correlation test; Kendall & Gibbons 1990).

In Figure 16, we see that it is the *overall* ISM density that is driving this trend, rather than the density of either the molecular gas, atomic gas, or dust components of the ISM alone, as all three have much weaker relationships with κ_{500} than is the case for the combined Σ_{ISM} . For Σ_{H_2} , $\tau_{M74} = -0.18$ and $\tau_{M83} = -0.55$; for Σ_d , $\tau_{M74} = -0.28$ and $\tau_{M83} = -0.42$; for Σ_{H_1} , $\tau_{M74} = 0.10$ and $\tau_{M83} = -0.34$.

The relationship between κ_{500} and gas-phase metallicity is plotted in Figure 15. Once again, whilst M83 shows no correlation, there does appear to be a trend for M74, with larger values of κ_{500} being associated with higher metallicities ($\mathcal{P}_{null} = 10^{-3.5}$ from a Kendall rank correlation test). On the one hand, metallicity is a parameter in Equation 3, so once again there is a definite risk of spurious correlations arising. However, if all other parameters in Equation 3 are held fixed, higher metallicity (therefore higher f_Z) leads to *lower* values of κ_{500} , meaning the trend for M74 in Figure 15 is being driven by the data in spite of this. Greater ISM metallicity will lead to increased grain growth (Dwek 1998; Zhukovska 2014; Galliano et al. 2018), and larger grains should give rise to larger values of κ_d (Li 2005; Köhler et al. 2015; Ysard et al. 2018).

We wished to assess whether local star formation has an effect on our calculated values of κ_{500} . There are several mechanisms by which recent star formation can process dust grains in its vicinity (see review in Galliano et al. 2018). For instance, photo-destruction by high-energy photons from massive (therefore young) stars can directly break down dust grains (Boulanger et al. 1998; Beirão et al. 2006), whilst the shocks produced by the supernovae of massive stars will sputter dust grains (Bocchio et al. 2014; Slavin et al. 2015). FUV emission should be a good proxy of these two environmental conditions; unobscured FUV emission is indicative of massive stars that are old enough to cleared their birth clouds, and hence represent the regions where supernovae will be occurring. And of course, regions with greater amounts of unobscured FUV emission demonstrably have an InterStellar Radiation Field (ISRF) with greater amounts of high-energy photons. If the environmental effects of recent star formation were impacting κ_{500} , this could manifest as a correlation with the total UV energy density, or with the UV energy density per dust mass (similar to the ‘heating parameter’ of Foyle et al. 2013), as the dust will be better shielded in areas with greater dust density. Therefore, in the two leftmost panels of Figure 17, we plot κ_{500} against both the GALEX Far-Ultraviolet (FUV) luminosity surface

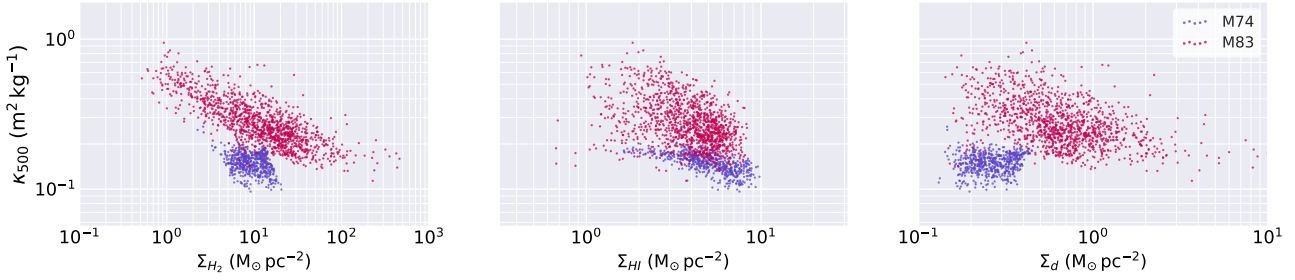


Figure 16. Plots of κ_{500} against the surface density of molecular gas (*left*), atomic gas (*centre*), and dust (*right*), for M74 and M83.

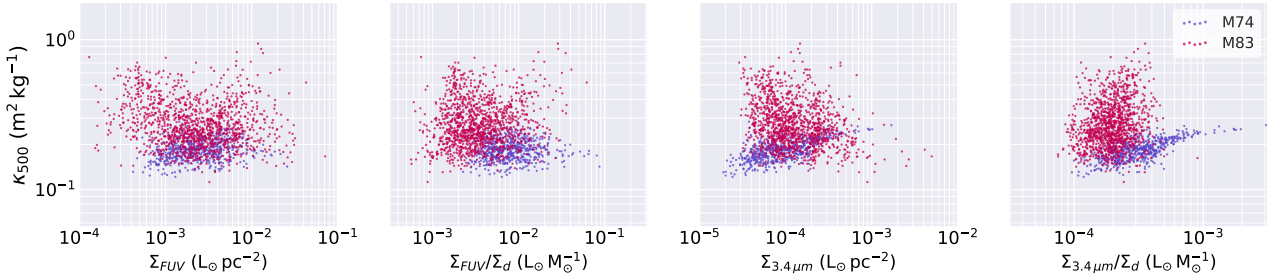


Figure 17. Plots of κ_{500} against the surface density of FUV luminosity surface density (1^{st}), FUV luminosity per dust mass (2^{nd}), $3.4\,\mu\text{m}$ luminosity surface density (3^{rd}), and $3.4\,\mu\text{m}$ luminosity per dust mass (4^{th}), for M74 and M83.

density¹⁹ (Σ_{FUV}), and against the FUV luminosity per dust mass surface density (Σ_{FUV}/Σ_d). No trend is apparent in either plot; M74, with its generally lower values of κ_{500} , has a higher average value of Σ_{FUV}/Σ_d , but this is to be expected given its bluer colours and lower submm surface brightness (see Table 1).

We also wished to assess whether the ISRF arising from evolved stars could be influencing κ_{500} , given that radiation from evolved stars can be the dominant source of energy received by dust in certain environments (Boquien et al. 2011; Bendo et al. 2012; Nersesian *accepted*). Observations in the NIR provide a good tracer of the evolved stellar population, and the ISRF it produces. Therefore, as with FUV, we plot κ_{500} against the WISE $3.4\,\mu\text{m}$ luminosity surface density¹⁹ ($\Sigma_{3.4\,\mu\text{m}}$), and against the $3.4\,\mu\text{m}$ luminosity per dust mass surface density ($\Sigma_{3.4\,\mu\text{m}}/\Sigma_d$), shown in the two right-most panels of Figure 17. In M74, it seems that the pixels with $\frac{\Sigma_{3.4\,\mu\text{m}}}{\Sigma_d} > 6 \times 10^{-4} L_\odot M_\odot^{-1}$ are exclusively associated with higher values of κ_{500} . And most interestingly, there is for both galaxies a positive correlation between κ_{500} and $\Sigma_{3.4\,\mu\text{m}}/\Sigma_d$. Whilst there is appreciable scatter, a Kendall rank correlation test gives $\mathcal{P}_{null} > 0.023$ for both – so it seems that this relationship, whilst broad, has probably not arisen by chance²⁰. Plus, the WISE $3.4\,\mu\text{m}$ data played no part in our κ_{500} calculations, making it hard to see how this relation could have arisen spuriously from our methodology.

A downside to using $500\,\mu\text{m}$ as the reference wavelength

is that carbonaceous species are expected to have considerably larger κ_{500} values than silicate species at these longer wavelengths (due to the steeper β for silicates; Ysard et al. 2018). Whereas at shorter wavelengths, the difference in κ_d between carbonaceous and silicate dust is smaller. Thus the choice of the longer reference wavelength might be limiting our ability to use the κ_d maps to trace such compositional variation. We therefore also produced versions of our κ_d maps at a reference wavelength of $160\,\mu\text{m}$. These κ_{160} maps are presented in Appendix E; however, they exhibit no difference in structure to the κ_{500} maps.

6 DISCUSSION

6.1 Robustness of Findings

Within M74 and M83, we find values of κ_{500} that vary by factors of 2.3 and 5.3 respectively. This is, to our knowledge, the first observational mapping of variation in κ_d within other galaxies. However, it is important to critically evaluate how much of this apparent variation could simply be an artefact of our method.

In a companion study to this work, Bianchi et al. (*in prep.*) use the dust-to-metals method to calculate global κ_d values for 204 DustPedia galaxies. As that study uses integrated gas measurements, they are unable to directly constrain ISM density. However, they do find that galaxies with higher H_2/HI ratios (typically associated with denser ISM) tend to have lower values of κ_d . This is what would be expected if the anticorrelation we find between κ_d and Σ_{ISM} continues on global scales, between galaxies. They also find large (a factor of several) scatter in their κ_d values between galaxies; in this context, the differences between the values we find for M73 and M83 are not conspicuous.

¹⁹ Maps were reprojected to the same pixel grid as the κ_{500} maps, then background-subtracted in the same manner as the continuum maps in Section 4.1. We manually masked pixels containing obvious foreground Milky Way stars.

²⁰ Spearman and Pearson rank correlation tests similarly both give $\mathcal{P}_{null} < 0.025$, with correlation coefficients > 0.2 .

Our key assumption of a fixed dust-to-metals ratio, ϵ_d , deserves particular scrutiny. As mentioned in Section 2, the vast majority of directly-measured²¹ values of ϵ_d lie in the range 0.2–0.6. Whilst this factor of 3 variation could notionally, in the worse-case-scenario, be sufficient to nullify the factor 2.3 variation in κ_d we find in M74, it could not nullify the factor 5.3 variation in M83. Moreover, as we show in Section 6.2.1, in the physically most likely scenario where ϵ_d scales with density, the variation in κ_{500} actually increases. Nonetheless, it is undoubtedly worth considering how, precisely, different kinds of systematic variations in ϵ_d within our target galaxies could be influencing our results.

There is evidence that ϵ_d is significantly reduced at low metallicities (Galliano et al. 2005; De Cia et al. 2016; Wiseman et al. 2017). However, there appears to be reduced variation in ϵ_d at intermediate-to-high metallicity. De Cia et al. (2016) and Wiseman et al. (2017) use depletions in damped Lyman- α absorbers to find only a factor of ~ 2 variation in ϵ_d at metallicities above $0.1 Z_\odot$, with at most a weak dependence on metallicity in that regime. Given that our analysis is concerned only with environments at $\gg 0.1 Z_\odot$, our results should be minimally susceptible to this scale of metallicity effect. Additionally, it should be noted that a number of studies have used visual extinction per column density of metals as a proxy for ϵ_d , and found it to be constant down to metallicities of $0.01 Z_\odot$, over a redshift range of $0.1 < z < 6.3$ (Watson 2011; Zafar & Watson 2013; Sparre et al. 2014).

A number of simulations have addressed the question of how ϵ_d varies. McKinnon et al. (2016) trace ϵ_d in cosmological zoom-in simulations, finding it varies by up to a factor of ~ 3.5 in the modern universe; however, they find minimal systematic variation within galaxies, except for enhanced values in galactic centres (see their Figures 1, 2, and 14). Popping et al. (2017) trace ϵ_d in semi-analytic models, and find that it can vary with metallicity by up to a factor of ~ 2 at metallicities $> 0.5 Z_\odot$ (with the degree and nature of this variation depending considerably upon the specific model).

However, if ϵ_d does indeed vary significantly with metallicity within our target galaxies, that will actually *increase* the amount of variation in κ_{500} in M83. The highest metallicities are at the inner regions of the disc, where κ_{500} is already lowest; if increasing f_Z in Equation 3 also increases ϵ_d , then this will drive down κ_d still further. On the other hand, because the lowest values of κ_d in M74 are found in the spiral arms, away from the centre, a correlation of ϵ_d with metallicity could indeed suppress some variation in κ_{500} – although M74 already exhibits a much smaller range in κ_{500} than M83.

Theoretical dust models can make specific predictions about how ϵ_d is expected to vary in different conditions. For instance, the THEMIS model traces how dust populations are expected to change in different interstellar environments, predicting that ϵ_d will increase monotonically with ISM density by a factor of ~ 3.5 , from 0.27 in the diffuse ISM ($n_H = 10^3 \text{ cm}^{-3}$) to 0.88 in the dense ISM ($n_H = 10^6 \text{ cm}^{-3}$),

driven by the accretion of gas-phase metals onto grains (Jones 2018). We explore the potential effects of this in detail in Section 6.2.1, where we find that it would further increase the variation in κ_{500} .

There are several observational studies that report variation of ϵ_d between and within galaxies, inferred from the fact that the gas-to-dust ratio is found to vary with metallicity (Rémy-Ruyer et al. 2014; Chiang et al. 2018; De Vis et al. 2019). However, these studies all rely upon an assumed value of κ_d to infer dust masses, and hence ϵ_d . Given that we, conversely, use an assumed ϵ_d to infer κ_d , it is not really possible to compare such results with ours in a valid way. However, we note with interest that these studies tend to find much larger ranges of ϵ_d than are suggested by either depletions, simulations, or theoretical dust models – up to 1 dex of scatter at a given metallicity, with up to 3 dex total range over all metallicities. One way to explain this discrepancy would be if κ_d is depressed at lower metallicity (which is potentially hinted at for M74 in Figure 15).

Beside a breakdown in our assumption of a fixed ϵ_d , it is possible that our method is being corrupted by the presence of ‘dark gas’ – H_2 at intermediate densities that CO fails to trace (Reach et al. 1994; Grenier et al. 2005; Wolfire et al. 2010). The presence of dark gas would have the effect of causing us to underestimate the value of M_{H_2} in Equation 3, thereby artificially driving up κ_{500} . The elevated areas of κ_{500} in our maps are indeed mainly associated with the inter-arm regions, where the fraction of dark gas is expected to be greatest (Langer et al. 2014; Smith et al. 2014). Estimates of the fraction of galactic gas mass that is dark range from 0% from dust and gas observations in M31 (Smith et al. 2012), to 30% in theoretical models (Wolfire et al. 2010), to 42% in hydrodynamical simulations of galactic discs (Smith et al. 2014), to 10–60% from *Planck* observations of the Milky Way (Planck Collaboration et al. 2011), to 6–60% from Milky Way γ -ray absorption studies (Grenier et al. 2005). Even assuming a worst-case scenario of a 60% dark gas fraction for the inter-arm regions of our target galaxies (an extreme scenario, given that the 60% represents the single largest fraction amongst the wide range of values reported within the Milky Way), dark gas could only reduce the variation in κ_{500} we find by a factor of 1.7.

In a similar vein, another potential confounder would be systematic variation in α_{CO} . If α_{CO} increases in denser ISM (*independent of metallicity*, which we account for), then this could counteract the variation in κ_d we find. However, evidence to date does not indicate that α_{CO} varies systematically in this way (Sandstrom et al. 2013). This of course could be due to the fact that the uncertainty on α_{CO} (and the scatter on the relations used to derive it) is large – however this uncertainty is propagated through our calculations.

In the course of determining κ_{500} for each pixel, values for the gas-to-dust ratio, G/D , are also generated. We find $176 < G/D < 277$ for M74, and $140 < G/D < 275$ for M83. Note that these are the ratios of *total* gas mass to dust mass. In the literature, quoted G/D values are often *hydrogen* to dust ratios (ie, no factor of ξ is applied to account for the masses of helium and metals); our hydrogen-to-dust ratios, G_H/D , are $127 < G_H/D < 201$ for M74, and $100 < G_H/D < 196$. For high-metallicity systems such as of our target galaxies, these are normal values when compared to the literature (Sandstrom et al. 2013; Rémy-Ruyer et al.

²¹ By ‘direct’, we refer to those measurements where ϵ_d is determined from observing the mass fraction of metals depleted from the gas phase.

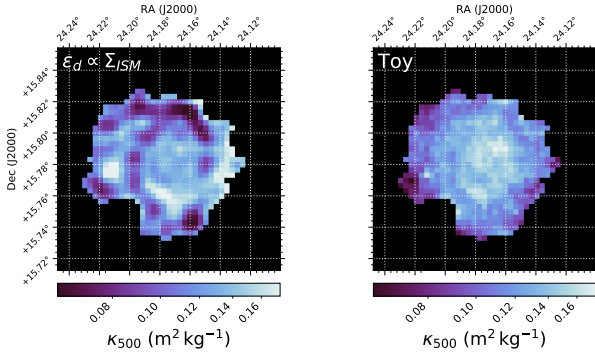


Figure 18. Maps of κ_{500} within M74, calculated using different model assumptions than for our fiducial map in Figure 12. *Left:* With the dust-to-metals ratio, ϵ_d , set to vary linearly as a function of Σ_{ISM} . *Right:* With a toy model where α_{CO} , $r_{2:1}$, T_d , β , ϵ_d , and $[12 + \log_{10} \frac{O}{H}]$ are kept constant.

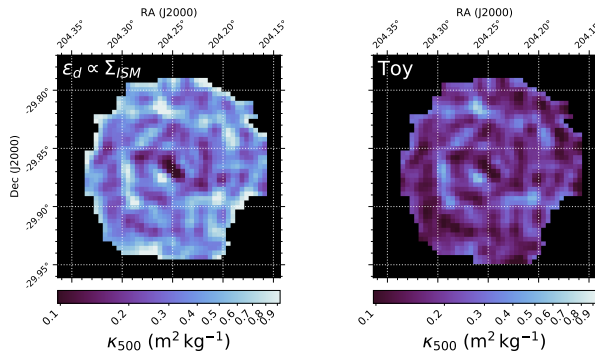


Figure 19. Maps of κ_{500} within M83, each calculated using different model assumptions than for our fiducial map in Figure 13. Model descriptions the same as for Figure 18.

2015; De Vis et al. 2017b). Indeed, we neatly reproduce the factor of 2–3 radial variation in G_H/D in M74 reported by Vázquez et al. (2019) and Chiang et al. (2018) over the 8.35–8.60 ($12 + \log_{10}[\frac{O}{H}]$) metallicity range we sample; although their adoption of fixed κ_d limits the scope for detailed comparison. Nonetheless we can say that our inferred dust masses yield sensible G/D values, following expected trends.

Overall, we are confident that our finding of an inverse correlation of κ_{500} is indeed robust against a wide range of changes to the initial assumptions of our method.

6.2 Alternate Models

6.2.1 Variable Dust-To-Metals Ratio

As discussed in Section 2, the assumption of a fixed ϵ_d is a simplification. Observed depletions in nearby portions of the Milky Way’s diffuse ISM indicate that in reality, ϵ_d increases with column density (Jenkins 2009; Draine et al. 2014; Roman-Duval et al. 2019). However, the form of this relation in extragalactic systems, where only integrated column density data is available, is not well constrained. Nonetheless, we can still explore, in general terms, how such a model would affect the manner in which κ_d scales. Even if this ap-

proach requires more assumptions, it may be more physical than our fiducial model.

We therefore repeated our κ_{500} mapping, setting ϵ_d to vary linearly as a function of Σ_{ISM} , with $\epsilon_d = 0.75$ at the point in each galaxy where Σ_{ISM} is highest, and $\epsilon_d = 0.25$ at the point where Σ_{ISM} is lowest. This specific choice of relationship is effectively arbitrary, but approximates the trend reported by Chiang et al. (2018) within M101, whilst also matching the range of ϵ_d values reported by De Vis et al. (2019) (although both of these sets of ϵ_d values were calculated with FIR-submm data, using an assumed value of κ_d , limiting scope for direct comparison).

The κ_{500} maps produced using the $\epsilon_d \propto \Sigma_{ISM}$ model are shown in the left panels of Figures 18 and 19, for M74 and M83 respectively. The trend of κ_{500} being depressed in the denser environments of the spiral arms remains. In fact, the anticorrelation between κ_{500} against Σ_{ISM} is even more exaggerated than was the case for our fiducial model, as can be seen in the left panel of Figure 20. The Kendall rank correlation coefficients for the $\epsilon_d \propto \Sigma_{ISM}$ results are more strongly negative than those of the fiducial version, being $\tau = -0.66$ for both M74 and M83. The range of κ_{500} values when using the $\epsilon_d \propto \Sigma_{ISM}$ model increases to a factor 5 in M74, and to a factor of 20 in M83.

It appears that our choice of fixed ϵ_d in our fiducial model actually serves to *reduce* the variation in κ_{500} , and that the (probably) more-physical $\epsilon_d \propto \Sigma_{ISM}$ model suggests a notably greater range of values. This increases our confidence that the variation in κ_{500} we see is a real effect. Whilst we could, for instance, construct a model where ϵ_d *decreases* with ISM density by a factor of > 5.3 , this would be completely unphysical, and would represent an entirely contrived attempt to minimise the κ_d variation we find. Similarly, we could construct a model where ϵ_d *increases* with radius – but whilst this would decrease the κ_d variation in M83, it would increase it for M74 (and would again be an unphysical contrivance).

6.2.2 ‘Toy’ Model

To establish the degree to which our results might simply be an artefact of our method, we again repeated our κ_{500} mapping, using a ‘toy’ model. For this repeat, metallicity was fixed at the Solar value of $12 + \log_{10}[\frac{O}{H}] = 8.69$, α_{CO} was fixed at the standard Milky Way value of $3.2 \text{ K}^{-1} \text{ km}^{-1} \text{ pc}^{-2}$, $r_{2:1}$ was fixed at the local-Universe average of 0.7, T_d was fixed at 20 K, β was fixed at 2, and ϵ_d was fixed at 0.4. Although this toy model is unphysical, it strips out as many assumptions as possible – allowing us to be confident that any trends that persist are not due to our GPR metallicity mapping, our SED fitting, our $r_{2:1}$ prescription, etc.

The κ_{500} maps produced using the toy model are shown in the right panels of Figures 18 and 19, for M74 and M83 respectively. The corresponding plot of κ_{500} against Σ_{ISM} is shown in the right panel of Figure 20, where it can be seen that the scatter is markedly increased for both galaxies. For M83, the trend is nonetheless still present, with a Kendall rank correlation test giving $\mathcal{P}_{null} < 10^{-5}$; the lowest values of κ_{500} are still visibly associated with the largest values of Σ_{ISM} , and vice-a-versa. For M74, the correlation of κ_{500} with Σ_{ISM} is lost; however the far smaller dynamic range in ISM density for this galaxy made it more susceptible to the

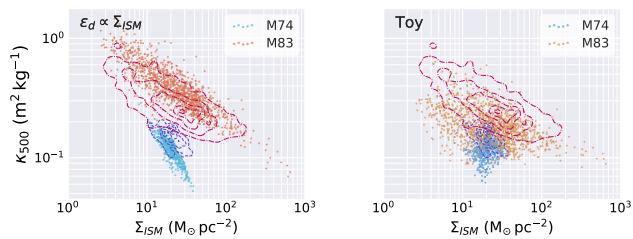


Figure 20. Alternate versions of Figure 14, again plotting κ_{500} against ISM surface density for M74 and M83, but for κ_{500} calculated using different model assumptions than for our fiducial method. Model descriptions the same as for Figure 18. For comparison, the distributions for our fiducial maps, as plotted in Figure 14, are indicated with contours (showing the 5th, 25th, 50th, 75th, and 95th percentiles); M74 as blue dashed, M83 as red dot-dashed.

trend being removed by the toy model’s increase in scatter. The fact the trend with ISM density persists for M83 despite the use of the toy model is extremely informative. It implies that the basic negative correlation is being driven by the interplay between the 21 cm data, CO data, and 500 μ m data – not by the specifics of our method.

6.2.3 Other Alternate Models

To provide further methodological checks, we produced additional alternate κ_{500} maps. In Appendix F, we present κ_{500} maps generated using metallicities calculated via different strong-line prescriptions than the one employed for our fiducial κ_{500} maps. In Appendix G, we present κ_{500} maps generated fitting a two-component MBB model to the FIR–submm fluxes, as opposed to the one-component MBB model used for our fiducial κ_{500} maps. In all cases the resulting κ_{500} maps display the same general morphology as our fiducial ones, with lower values of κ_{500} associated with denser regions.

6.3 Implications of Findings

Our finding that κ_{500} shows a strong negative correlation with ISM density is in direct contradiction to standard models of dust emission, which predict that the densest regions of the ISM should exhibit the highest values of κ_d (Ossenkopf & Henning 1994; Li & Lunine 2003; Jones 2018) bsphack-esphack. This expectation arises from the fact that dust grains in the densest parts of the ISM are predicted to be larger, due to the coagulation of grains and the growth of (icy) mantles on their surfaces, and that larger grains should be more emissive per unit mass (Köhler et al. 2012; Jones et al. 2013; Ysard et al. 2018). The apparent incompatibility of our results with these predictions presents one of two possibilities.

The first possibility is that our method has some fundamental flaw that has systematically affected the results. We have made an effort to construct our method so that it only relies upon standard, widely-used assumptions. If one (or more) of these assumptions breaks down systematically, in a manner such that the bias is a function of ISM density, and the bias is a factor of > 5 , then this could give rise to the results we see. We have tried to inoculate our findings

against even this scenario (for instance, by trying the toy model where all possible variables were kept fixed). However if, for example, dark gas represents 75% of the total gas mass in inter-arm space (artificially suppressing our assumed M_{H_2}), this could negate our results for M74. If dark gas represents 75% of the total gas mass in inter-arm space if *and* if HII region oxygen depletion were a factor of 2 lower in inter-arm space versus other metals (compromising its use as a metallicity tracer), then our results for M83 could be negated – however scenarios this extreme are unlikely, being unprecedented in the literature, and would have significant implications for extragalactic studies in general.

The second possibility is that κ_{500} truly does decrease in denser ISM. This would help explain some observational results. For instance, an excess in submm emission has been found in lower-density areas within galaxies (Relaño et al. 2018), and within galaxies dominated by diffuse regions (Lamperti et al. *in prep.*; De Looze et al. *in prep.*); if κ_{500} is indeed elevated in low-density regions, it could give rise to this effect.

It is hard to explain decreasing κ_{500} in denser ISM in the context of current dust physics. However it is possible to construct scenarios where it is not entirely unreasonable. Ysard et al. (2018) present a detailed exploration of how changes in various physical parameters of dust should affect κ_d . For instance, spherical grains are predicted to have lower κ_{500} than oblate or prolate grains, by up to a factor of ~ 1.5 (see their Figure 5); and hydrogenated amorphous carbon grains are expected to have much lower κ_{500} than amorphous silicate or unhydrogenated amorphous carbon grains (by up to an order magnitude). Whilst we do not suggest that this (or any other) specific physical scenario is the cause of our observed trend, it demonstrates that it is at least possible to envisage an evolution in dust properties that does not entail an uninterrupted monotonic increase in κ_d with ISM density.

On that theme, we also note that our data only provides physical resolution of 590 pc pix^{-1} in M74 and 330 pc pix^{-1} in M83. As such, we can do no better than distinguish between arm and inter-arm pixels. This will have ‘smeared out’ the properties of the denser clouds within the spiral arms. When studies discuss grain growth in the dense ISM, and the associated increases in κ_d , the dense medium in question is typically described as having at least 1500–10000 $n_H \text{ cm}^{-3}$, compared to 20–50 $n_H \text{ cm}^{-3}$ in the diffuse ISM (Ferrière 2001; Köhler et al. 2015; Jones 2018) – a difference in density of at least a factor of 30. However, our data only traces a dynamic range in density of a factor of 5 in M74, and a factor of 50 in M83 (discounting pixels within 1 beam of the nuclear starburst, where our κ_{500} values become unreliable, as per Section 5). So whilst we are probing a wide range of ISM conditions, we are unable to perform a ‘clean’ sampling of the densest grain-growth environments. Likewise, we only performed our analysis for pixels with sufficient SNR for all data – thereby excluding regions of particularly low ISM density, especially at the outskirts of the target galaxies. As such, it seems likely that, in practice, we are effective probing intermediate density environments.

Some grain models do indeed predict that κ_{500} should drop at intermediate densities, before increasing again at the highest densities. For example, the Köhler et al. (2015) description of the THEMIS model finds that the grain-mixture-

average κ_{500} should *fall* by a factor of 2.3 (relative to the diffuse ISM) for grains undergoing accretion at intermediate densities ($1500 n_{\text{H}} \text{ cm}^{-3}$) – with κ_{500} falling by a factor of 26 for amorphous carbon grains in particular. Then at even higher densities, as grains start to aggregate, κ_{500} will increase again, becoming even higher in the densest regions where icy mantles can form. Again, we do not argue that these specific effects are what are responsible for the relationship we find (as we lack the density resolution, and *volume* density information, necessary to test this). However, THEMIS does demonstrate that it is possible to construct a physical dust framework where κ_{500} falls as Σ_{ISM} increases, over some intermediate transition regime.

It is also worth considering why our distribution of κ_{500} values for M 74 is offset from that of M 83, by about 0.3 dex. The most obvious difference in the properties of the two galaxies is the greater ISM surface density of M 83; but given the apparent anti-correlation of κ_{500} with Σ_{ISM} , this seems unlikely to be the driver of the in κ_{500} . M 83 has almost 3 times the star formation rate of M 73 (Nersesian et al. 2019), despite being physically more compact (see Table 1), giving it an average star formation rate surface density that is >6 times greater. Despite this, M 74 has bluer colours, and the relative scale-lengths of the dust and stars in M 74 and M 83, as reported in Casasola et al. (2017), differ considerably – in M 74, the dust and gas have very different scale lengths ($2.35'$ vs $1.04'$), whereas in M 83, the dust and gas scale lengths are effectively identical ($1.66'$ vs $1.68'$). So there is clearly a difference in the relative geometries of the stars and ISM in these galaxies. When comparing resolved observations of spiral galaxies, it is well established that there can be appreciable differences in ISM properties, even at a given surface density (Usero et al. 2015; Gallagher et al. 2018; Sun et al. 2018). Therefore, it is not necessarily surprising that κ_d may also have different values in different galaxies, at a given surface density.

X-ray observations of M 74 and M 83 indicate that their interstellar media contain diffuse hot gas components (Owen & Warwick 2009) that span much of their discs. Such gas could process the dust in a galaxy, sputtering the grains, and (in standard models) therefore decreasing the grains' κ_d (Galliano et al. 2018). That said, we find decreased κ_d in the denser ISM, where grains should be more shielded from X-ray gas. Nonetheless, it is possible that the trends we find may not be applicable to galaxies with less prominent X-ray gas content.

7 CONCLUSION

Using a homogenous dataset assembled as part of the DustPedia project (Davies et al. 2017), we have produced the first maps of the dust mass absorption coefficient, κ_d , within two nearby galaxies: M 74 (NGC 628) and M 83 (NGC 5236).

Our method for finding κ_d is empirical, and avoids making any assumptions about the composition or radiative properties of the dust. Instead, our approach exploits the fact that the ISM dust-to-metals ratio seems to exhibit minimal variation at high metallicity. With this one assumption, we can use gas and metallicity data to determine dust masses *a priori*; by comparing these masses to observed dust emission, we are able to calibrate values for κ_d . Given that the

value of the dust-to-metals ratio is much less uncertain than the value of κ_d , we are able to leverage the one to explore the other.

As a proof-of-concept demonstration, we have applied this method on a resolved, pixel-by-pixel basis to M 74 and M 83, two nearby face-on spiral galaxies, that have well-suited atomic gas, molecular gas, dust emission, and ISM metallicity data available. We have produced gas-phase metallicity maps for these galaxies, using the many hundreds of available spectra measurements, via a novel application of Gaussian process regression, with which we infer the underlying metallicity distribution.

We find strong evidence for significant variation in κ_{500} within both galaxies – by a factor of 2.3 within M 74 ($0.11\text{--}0.25 \text{ m}^2 \text{ kg}^{-1}$), and by a factor of 5.3 within M 83 ($0.15\text{--}0.80 \text{ m}^2 \text{ kg}^{-1}$).

We examine whether κ_d shows variation with other measured and derived properties of the target galaxies. We find that κ_d exhibits a distinct negative correlation with the surface density of the ISM, following a power law slope of index $-0.36^{+0.26}_{-0.21}$ (although the power-laws for the two galaxies are offset by 0.3 dex). This trend appears to be dictated by the total ISM surface density, as opposed to the surface density of either its atomic, molecular, or dust components. This trend is the opposite of what is predicted by most dust models. However, the relationship is robust against a wide range of changes to our method – only the adoption of unphysical or highly unusual assumptions would be able to suppress it. We discuss possible ways of reconciling this finding with the current understanding of dust physics – such as the possibility that our combination of resolution and sensitivity means that we biased towards probing regimes of intermediate density where the broader expected correlation between density and κ_d may not hold true.

We also find tentative indications of correlation of κ_d with other properties, such as metallicity, NIR radiation field intensity, and dust emissivity slope β . However, the evidence for these is less conclusive (and some of these parameters were inputs to our κ_d calculations), so we are more cautious about the significance of these relationships.

This study lays the groundwork for a wide range of future work. An expanded study of resolved κ_d is possible with the DustPedia dataset, but at present the availability of well-resolved metallicity data would limit it to a sample of only 10–20 galaxies. But in future, large IFU surveys of highly-extended nearby galaxies, especially the SDSS-V Local Volume Mapper (Kollmeier et al. 2017) will dramatically improve this situation. Simultaneously, data now exists to apply the dust-to-metals method to large, statistical samples of galaxies on a global basis; in particular, the JCMT dust and gas In Nearby Galaxies Legacy Exploration (JINGLE, Saintonge et al. 2018), which is assembling consistent high-quality CO, HI, dust, and IFU data for almost 200 galaxies, would be well-suited to this task.

Most importantly, many of the questions raised could be tackled by conducting a similar analysis at improved spatial resolution. For this reason, we have begun work on applying this method as part of an analysis of several Local Group galaxies – including the Large and Small Magellanic Clouds, where we enjoy particularly exquisite resolution. Most significantly, better resolution will allow us to cleanly probe a larger range of density, from the densest grain-grown re-

gions, down to the most diffuse ISM. We will thereby test if the surprising anticorrelation between κ_{500} and Σ_{ISM} holds true. Another benefit to expanding our analysis to the Magellanic Clouds is that they are the subjects of ongoing work to perform the first extragalactic depletion analyses (Jenkins & Wallerstein 2017; Roman-Duval et al. 2019). Exploiting that data will allow us to use in-situ measurements of the dust-to-metal ratio, removing the single largest source of uncertainty we presently face, and allowing us to produce the most reliable empirical κ_d determinations available with current data.

ACKNOWLEDGEMENTS

The DustPedia project²² (Davies et al. 2017) has received funding from the European Union’s Seventh Framework Programme (FP7) for research, technological development, and demonstration, under grant agreement 606824 (PI Jon Davies).

The authors thank the anonymous referee whose comments have materially improved the quality of this work.

CJRC acknowledges financial support from NASA Astrophysics Data Analysis Program (ADAP) grant 80NSSC18K0944. CJRC thanks Andreas Lundgren and Tommy Wiklund for providing reduced SEST CO data for M83 (Lundgren et al. 2004). CJRC also thanks Philip Wiseman, Bruce Draine, Julia Roman-Duval, Karl Gordon, Rosie Beeston, and Phil Cigan for helpful discussions & input.

This research made use of Astropy²³, a community-developed core Python package for Astronomy (Astropy Collaboration et al. 2013, 2018). This research made use of Astropy²⁴, an Astropy-affiliated Python package for accessing remotely hosted astronomical data (Ginsburg et al. 2019). This research made use of Reproject²⁵, an Astropy-affiliated Python package for image reprojection. This research has made use of NumPy²⁶ (van der Walt et al. 2011), SciPy²⁷ (Jones et al. 2001), and Matplotlib²⁸ (Hunter 2007). This research made use of APLpy²⁹, an open-source plotting package for Python (Roitaille & Bressert 2012). This research made use of the Pandas³⁰ data structures package for Python (McKinney 2010). This research made use of the scikit-image³¹ image processing package for Python and the scikit-learn³² machine learning package for Python (Pedregosa et al. 2011). This research made use of emcee³³, the MCMC hammer for Python (Foreman-Mackey et al. 2013). This research made use of the PyMC3³⁴ MCMC package for Python. This research made use of the corner³⁵ scatterplot matrix plotting package for Python (Foreman-Mackey 2016). This research made use of iPython, an enhanced interactive Python (Pérez & Granger 2007). This research made use of Python code for working in the luminance-chroma-hue colour space, written

by Endolith³⁶, kindly made available free and open-source under the BSD License³⁷, and copyright 2014 Endolith.

This research has made use of TOPCAT³⁸ (Taylor 2005), an interactive graphical viewer and editor for tabular data, which was initially developed under the UK Starlink project, and has since been supported by PPARC, the VOTech project, the Astro-Grid project, the AIDA project, the STFC, the GAVO project, the European Space Agency, and the GENIUS project. This research made use of ds9, a tool for data visualisation supported by the Chandra X-ray Science Center (CXC) and the High Energy Astrophysics Science Archive Center (HEASARC) with support from the JWST Mission office at the Space Telescope Science Institute for 3D visualisation.

This research made use of Montage³⁹, which is funded by the National Science Foundation under Grant Number ACI-1440620, and was previously funded by the National Aeronautics and Space Administration’s Earth Science Technology Office, Computation Technologies Project, under Cooperative Agreement Number NCC5-626 between NASA and the California Institute of Technology.

This research made use of the Vizier catalogue access tool⁴⁰ (Ochsenbein et al. 2000), operated at CDS, Strasbourg, France. This research has made use of the NASA/IPAC Extragalactic Database⁴¹ (NED), operated by the Jet Propulsion Laboratory, California Institute of Technology, under contract with the National Aeronautics and Space Administration.

This research made use of data from the Swedish-ESO Submillimetre Telescope, which was operated jointly by ESO and the Swedish National Facility for Radio Astronomy, Chalmers University of Technology.

Much of the model fitting performed in this work benefitted from the invaluable guidance provided in Hogg et al. (2010).

REFERENCES

- Accurso G., et al., 2017, *MNRAS*, **470**, 4750
- Agladze N. I., Sievers A. J., Jones S. A., Burlitch J. M., Beckwith S. V. W., 1996, *ApJ*, **462**, 1026
- Alton P. B., Xilouris E. M., Misiriotis A., Dasyra K. M., Dumke M., 2004, *A&A*, **425**, 109
- Amorín R., Muñoz-Tuñón C., Aguerri J. A. L., Planesas P., 2016, *A&A*, **588**, A23
- Angus R., Morton T., Aigrain S., Foreman-Mackey D., Rajpaul V., 2018, *MNRAS*, **474**, 2094
- Asplund M., Grevesse N., Sauval A. J., Scott P., 2009, *ARA&A*, **47**, 481
- Astropy Collaboration et al., 2013, *A&A*, **558**, A33
- Astropy Collaboration et al., 2018, *AJ*, **156**, 123
- Aver E., Olive K. A., Porter R. L., Skillman E. D., 2013, *J. Cosmology Astropart. Phys.*, **11**, 17
- Bacon R., et al., 2010, in Ground-based and Airborne Instrumentation for Astronomy III. p. 773508, doi:10.1117/12.856027
- Balog Z., et al., 2014, *Experimental Astronomy*, **37**, 129
- Balser D. S., 2006, *AJ*, **132**, 2326
- Beirão P., Brandl B. R., Devost D., Smith J. D., Hao L., Houck J. R., 2006, *ApJ*, **643**, L1
- Bendo G. J., et al., 2012, *MNRAS*, **419**, 1833
- Bendo G. J., et al., 2013, *MNRAS*, **433**, 3062
- 36 <https://gist.github.com/endolith/5342521>
- 37 <https://opensource.org/licenses/BSD-3-Clause>
- 38 <http://www.star.bris.ac.uk/~mbt/topcat/>
- 39 <https://montage.ipac.caltech.edu/>
- 40 <https://vizier.u-strasbg.fr/viz-bin/VizieR>
- 41 <https://ned.ipac.caltech.edu/>

²² <https://dustpedia.com/>

²³ <https://www.astropy.org/>

²⁴ <https://astroquery.readthedocs.io>

²⁵ <https://reproject.readthedocs.io>

²⁶ <https://numpy.org/>

²⁷ <https://scipy.org/>

²⁸ <https://matplotlib.org/>

²⁹ <https://aplpy.github.io/>

³⁰ <https://pandas.pydata.org/>

³¹ <https://scikit-image.org/>

³² <https://scikit-learn.org>

³³ <https://dfm.io/emcee/current/>

³⁴ <https://docs.pymc.io/>; Salvatier et al. 2016

³⁵ <https://corner.readthedocs.io>

- Berg D. A., Skillman E. D., Croxall K. V., Pogge R. W., Moustakas J., Johnson-Groh M., 2015, *ApJ*, **806**, 16
- Berg D. A., Skillman E. D., Henry R. B. C., Erb D. K., Carigi L., 2016, *ApJ*, **827**, 126
- Bianchi S., et al., 2017, *A&A*, **597**, A130
- Bigiel F., et al., 2011, *ApJ*, **730**, L13
- Blanc G. A., et al., 2013, *AJ*, **145**, 138
- Blanc G. A., Kewley L., Vogt F. P. A., Dopita M. A., 2015, *ApJ*, **798**, 99
- Bocchio M., Jones A. P., Slavin J. D., 2014, *A&A*, **570**, A32
- Bolatto A. D., Wolfire M., Leroy A. K., 2013, *Annual Review of Astronomy and Astrophysics*, **51**, 207
- Boquien M., et al., 2011, *AJ*, **142**, 111
- Boselli A., et al., 2010, *PASP*, **122**, 261
- Boulanger F., Perault M., 1988, *ApJ*, **330**, 964
- Boulanger F., et al., 1998, in Yun J., Liseau L., eds, *Astronomical Society of the Pacific Conference Series Vol. 132, Star Formation with the Infrared Space Observatory*. p. 15
- Bresolin F., Kudritzki R.-P., Urbaneja M. A., Gieren W., Ho I. T., Pietrzyński G., 2016, *ApJ*, **830**, 64
- Buat V., et al., 2005, *ApJ*, **619**, L51
- Burgarella D., Buat V., Iglesias-Páramo J., 2005, *MNRAS*, **360**, 1413
- Casasola V., Hunt L., Combes F., García-Burillo S., 2015, *A&A*, **577**, A135
- Casasola V., et al., 2017, *A&A*, **605**, A18
- Casoli F., Dupraz C., Combes F., Kazes I., 1991, *A&A*, **251**, 1
- Chastenot J., Bot C., Gordon K. D., Bocchio M., Roman-Duval J., Jones A. P., Ysard N., 2017, *A&A*, **601**, A55
- Chiang I. D., Sandstrom K. M., Chastenot J., Johnson L. C., Leroy A. K., Utomo D., 2018, *ApJ*, **865**, 117
- Ciesla L., et al., 2014, *A&A*, **565**, A128
- Clark P. C., Glover S. C. O., 2015, *MNRAS*, **452**, 2057
- Clark C. J. R., et al., 2015, *MNRAS*, **452**, 397
- Clark C. J. R., Schofield S. P., Gomez H. L., Davies J. I., 2016, *MNRAS*, **459**, 1646
- Clark C. J. R., et al., 2018, *A&A*, **609**, A37
- Clemens M. S., et al., 2013, *MNRAS*, **433**, 695
- Colbert J., 2011, *IRAC Instrument Handbook. MIPS Instrument and MIPS Instrument Support Teams*, 3.0 edn
- Compiègne M., et al., 2011, *A&A*, **525**, A103
- Cressie N., Wikle C. K., 2011, *Statistics for Spatio-temporal Data*, 1st edition edn. Wiley, Hoboken
- Cutri R. M., et al., 2012, Technical report, Explanatory Supplement to the WISE All-Sky Data Release Products
- Dasyra K. M., Xilouris E. M., Misiriotis A., Kylafis N. D., 2005, *A&A*, **437**, 447
- Davies J. I., et al., 2017, *PASP*, **129**, 044102
- De Cia A., Ledoux C., Savaglio S., Schady P., Vreeswijk P. M., 2013, *A&A*, **560**, A88
- De Cia A., Ledoux C., Mattsson L., Petitjean P., Srianand R., Gavignaud I., Jenkins E. B., 2016, *A&A*, **596**, A97
- De Vis P., et al., 2017a, *MNRAS*, **464**, 4680
- De Vis P., et al., 2017b, *MNRAS*, **471**, 1743
- De Vis P., et al., 2019, *A&A*, **623**, A5
- Decin L., Eriksson K., 2007, *A&A*, **472**, 1041
- Demyk K., et al., 2013, in *Proceedings of The Life Cycle of Dust in the Universe: Observations, Theory, and Laboratory Experiments (LCDU2013)*. 18-22 November, 2013. Taipei, Taiwan. Editors: Anja Andersen, Maarten Baes, Haley Gomez, Ciska Kemper, Darach Watson..
- Demyk K., et al., 2017a, *A&A*, **600**, A123
- Demyk K., et al., 2017b, *A&A*, **606**, A50
- Desert F.-X., Boulanger F., Puget J. L., 1990, *A&A*, **237**, 215
- Draine B. T., 2003, *ARA&A*, **41**, 241
- Draine B. T., Li A., 2007, *ApJ*, **657**, 810
- Draine B. T., et al., 2007, *ApJ*, **663**, 866
- Draine B. T., et al., 2014, *ApJ*, **780**, 172
- Dunne L., et al., 2018, *MNRAS*, **479**, 1221
- Dwek E., 1998, *ApJ*, **501**, 643
- Eales S., et al., 2010a, *PASP*, **122**, 499
- Eales S. A., et al., 2010b, *A&A*, **518**, L62
- Eales S., et al., 2012, *ApJ*, **761**, 168
- Eisenstein D. J., et al., 2011, *AJ*, **142**, 72
- Elmegreen D. M., Elmegreen B. G., 1987, *ApJ*, **314**, 3
- Exter K., Balog Z., Cazoletti L., Klaas U., Lutz D., Paladini R., Puga E., Royer P., 2019, *PACS Handbook*. PACS Consortium and the PACS Instrument Control Centre, 4.0.1 edn
- Fathi K., et al., 2008, *ApJ*, **675**, L17
- Fazio G. G., et al., 2004, *ApJS*, **154**, 10
- Ferrière K. M., 2001, *Reviews of Modern Physics*, **73**, 1031
- Foreman-Mackey D., 2016, *The Journal of Open Source Software*, **1**, 24
- Foreman-Mackey D., Hogg D. W., Lang D., Goodman J., 2013, *Publications of the Astronomical Society of the Pacific*, **125**, 306
- Foyle K., et al., 2013, *MNRAS*, **432**, 2182
- Galametz M., et al., 2012, *MNRAS*, **425**, 763
- Gallagher M. J., et al., 2018, *ApJ*, **858**, 90
- Galliano F., 2018, *MNRAS*, **476**, 1445
- Galliano F., Madden S. C., Jones A. P., Wilson C. D., Bernard J.-P., 2005, *A&A*, **434**, 867
- Galliano F., Dwek E., Chanial P., 2008, *ApJ*, **672**, 214
- Galliano F., Galametz M., Jones A. P., 2018, *Annual Review of Astronomy and Astrophysics*, **56**, 673
- Garnett D. R., Skillman E. D., Dufour R. J., Peimbert M., Torres-Peimbert S., Terlevich R., Terlevich E., Shields G. A., 1995, *ApJ*, **443**, 64
- Gatti C. S., 2015, PhD thesis, Rensselaer Polytechnic Institute, doi:10.1007/978-3-319-12197-0
- Geweke J., 1992, in *IN BAYESIAN STATISTICS*. University Press, pp 169–193
- Ginsburg A., et al., 2019, *AJ*, **157**, 98
- Goodwin S. P., Gribbin J., Hendry M. A., 1998, *The Observatory*, **118**, 201
- Gordon K. D., et al., 2014, *ApJ*, **797**, 85
- Grenier I. A., Casandjian J.-M., Terrier R., 2005, *Science*, **307**, 1292
- Griffin M. J., et al., 2010, *A&A*, **518**, L3
- Griffin M. J., et al., 2013, *MNRAS*, **434**, 992
- Harris J., Calzetti D., Gallagher John S. I., Conselice C. J., Smith D. A., 2001, *AJ*, **122**, 3046
- Ho I. T., 2019, *MNRAS*, **485**, 3569
- Hogg D. W., Bovy J., Lang D., 2010, preprint, p. arXiv:1008.4686 (arXiv:1008.4686)
- Hunter J. D., 2007, *Computing in Science & Engineering*, **9**, 90
- Issa M. R., MacLaren I., Wolfendale A. W., 1990, *A&A*, **236**, 237
- Izotov Y. I., Guseva N. G., Fricke K. J., Krügel E., Henkel C., 2014, *A&A*, **570**, A97
- James A., Dunne L., Eales S., Edmunds M. G., 2002, *MNRAS*, **335**, 753
- Jenkins E. B., 2009, *ApJ*, **700**, 1299
- Jenkins E. B., Wallerstein G., 2017, *ApJ*, **838**, 85
- Jones A., 2013, in *Proceedings of The Life Cycle of Dust in the Universe: Observations, Theory, and Laboratory Experiments (LCDU2013)*. 18-22 November, 2013. Taipei, Taiwan. Editors: Anja Andersen, Maarten Baes, Haley Gomez, Ciska Kemper, Darach Watson..
- Jones A. P., 2018, arXiv e-prints, p. arXiv:1804.10628
- Jones E., Oliphant T., Peterson P., et al., 2001, *SciPy: Open source scientific tools for Python*, <http://www.scipy.org/>
- Jones A. P., Fanciullo L., Köhler M., Verstraete L., Guillet V., Bocchio M., Ysard N., 2013, *A&A*, **558**, A62
- Jones A. P., Köhler M., Ysard N., Dartois E., Godard M., Gavilan L., 2016, *A&A*, **588**, A43

- Jones A. P., Koehler M., Ysard N., Bocchio M., Verstraete L., 2017, preprint, ([arXiv:1703.00775](https://arxiv.org/abs/1703.00775))
- Juvela M., Ysard N., 2012, *A&A*, **539**, A71
- Kelly B. C., Shetty R., Stutz A. M., Kauffmann J., Goodman A. A., Launhardt R., 2012, *ApJ*, **752**, 55
- Kendall M. G., Gibbons J. D., 1990, Rank Correlation Methods, 5th edition edn. Griffin, London
- Kennicutt Jr. R. C., 1998, *ApJ*, **498**, 541
- Kennicutt Jr. R. C., et al., 2009, *ApJ*, **703**, 1672
- Kimura H., Mann I., Jessberger E. K., 2003, *ApJ*, **582**, 846
- Kirkpatrick A., et al., 2013, *ApJ*, **778**, 51
- Kirkpatrick A., et al., 2014, *ApJ*, **789**, 130
- Köhler M., Stepnik B., Jones A. P., Guillet V., Abergel A., Ristorcelli I., Bernard J. P., 2012, *A&A*, **548**, A61
- Köhler M., Ysard N., Jones A. P., 2015, *A&A*, **579**, A15
- Kollmeier J. A., et al., 2017, arXiv e-prints, p. [arXiv:1711.03234](https://arxiv.org/abs/1711.03234)
- Kudritzki R.-P., Urbaneja M. A., Gazak Z., Bresolin F., Przybilla N., Gieren W., Pietrzyński G., 2012, *ApJ*, **747**, 15
- Langer W. D., Velusamy T., Pineda J. L., Willacy K., Goldsmith P. F., 2014, *A&A*, **561**, A122
- Leroy A. K., et al., 2009, *AJ*, **137**, 4670
- Leroy A. K., et al., 2013, *AJ*, **146**, 19
- Li A., 2005, in Popescu C. C., Tuffs R. J., eds, American Institute of Physics Conference Series Vol. 761, The Spectral Energy Distributions of Gas-Rich Galaxies: Confronting Models with Data. pp 123–133 ([arXiv:astro-ph/0503567](https://arxiv.org/abs/astro-ph/0503567)), doi:10.1063/1.1913922
- Li A., Lunine J. I., 2003, *ApJ*, **590**, 368
- Lianou S., Xilouris E., Madden S. C., Barmby P., 2016, *MNRAS*, **461**, 2856
- Luck R. E., Lambert D. L., 1992, *ApJS*, **79**, 303
- Lundgren A. A., Wiklind T., Olofsson H., Rydbeck G., 2004, *A&A*, **413**, 505
- Malinen J., Juvela M., Collins D. C., Lunttila T., Padoan P., 2011, *A&A*, **530**, A101
- Marsh K. A., Whitworth A. P., Lomax O., 2015, *MNRAS*, **454**, 4282
- Marsh K. A., et al., 2017, *MNRAS*, **471**, 2730
- Mattsson L., De Cia A., Andersen A. C., Petitjean P., 2019, *A&A*, **624**, A103
- McKinney W., 2010, in van der Walt S., Millman J., eds, Proceedings of the 9th Python in Science Conference. pp 51 – 56
- McKinnon R., Torrey P., Vogelsberger M., 2016, *MNRAS*, **457**, 3775
- Mesa-Delgado A., Esteban C., García-Rojas J., Luridiana V., Bautista M., Rodríguez M., López-Martín L., Peimbert M., 2009, *MNRAS*, **395**, 855
- Meyer D. M., Jura M., Cardelli J. A., 1998, *ApJ*, **493**, 222
- Meyer M. J., et al., 2004, *MNRAS*, **350**, 1195
- Minasny B., McBratney A. B., 2005, *Geofísica Internacional*, **128**, 192
- Morrissey P., et al., 2007, *ApJS*, **173**, 682
- Moustakas J., Kennicutt Jr. R. C., Tremonti C. A., Dale D. A., Smith J.-D. T., Calzetti D., 2010, *ApJS*, **190**, 233
- Nersesian A., et al., 2019, *A&A*, **624**, A80
- Noll S., Burgarella D., Giovannoli E., Buat V., Marcellac D., Muñoz-Mateos J. C., 2009, *A&A*, **507**, 1793
- Obreschkow D., Rawlings S., 2009, *MNRAS*, **394**, 1857
- Ochsenbein F., Bauer P., Marcout J., 2000, *A&AS*, **143**, 23
- Oliver S. J., et al., 2012, *MNRAS*, **424**, 1614
- Ormel C. W., Min M., Tielens A. G. G. M., Dominik C., Paszun D., 2011, *A&A*, **532**, A43
- Ossenkopf V., Henning T., 1994, *A&A*, **291**, 943
- Owen R. A., Warwick R. S., 2009, *MNRAS*, **394**, 1741
- Pedregosa F., et al., 2011, Journal of Machine Learning Research, **12**, 2825
- Peebles M. S., Werk J. K., Tumlinson J., Oppenheimer B. D., Prochaska J. X., Katz N., Weinberg D. H., 2014, *ApJ*, **786**, 54
- Pei Y. C., 1992, *ApJ*, **395**, 130
- Pei Y. C., Fall S. M., Hauser M. G., 1999, *ApJ*, **522**, 604
- Peimbert A., Peimbert M., 2010, *ApJ*, **724**, 791
- Pérez F., Granger B. E., 2007, *Computing in Science and Engineering*, **9**, 21
- Pettini M., Pagel B. E. J., 2004, *MNRAS*, **348**, L59
- Pettini M., Zych B. J., Steidel C. C., Chaffee F. H., 2008, *MNRAS*, **385**, 2011
- Pilbratt G. L., et al., 2010, *A&A*, **518**, L1
- Pilyugin L. S., Grebel E. K., 2016, *MNRAS*, **457**, 3678
- Planck Collaboration et al., 2011, *A&A*, **536**, A21
- Planck Collaboration et al., 2014, *A&A*, **571**, A11
- Poglitsch A., et al., 2010, *A&A*, **518**, L2
- Popping G., Somerville R. S., Galametz M., 2017, *MNRAS*, **471**, 3152
- Rasmussen C. E., Williams C. K. I., 2006, Gaussian Processes for Machine Learning, 5th edition edn. The MIT Press, London
- Reach W. T., Koo B.-C., Heiles C., 1994, *ApJ*, **429**, 672
- Regan M. W., Thornley M. D., Helfer T. T., Sheth K., Wong T., Vogel S. N., Blitz L., Bock D. C. J., 2001, *ApJ*, **561**, 218
- Relaño M., et al., 2018, *A&A*, **613**, A43
- Rémy-Ruyer A., et al., 2013, *A&A*, **557**, A95
- Rémy-Ruyer A., et al., 2014, *A&A*, **563**, A31
- Rémy-Ruyer A., et al., 2015, *A&A*, **582**, A121
- Rieke G. H., et al., 2004, *ApJS*, **154**, 25
- Rix H.-W., Bovy J., 2013, *Astronomy and Astrophysics Review*, **21**, 61
- Robitaille T., Bressert E., 2012, APLpy: Astronomical Plotting Library in Python, Astrophysics Source Code Library (ascl:1208.017)
- Roman-Duval J., Bot C., Chastenot J., Gordon K., 2017, *ApJ*, **841**, 72
- Roman-Duval J., et al., 2019, *ApJ*, **871**, 151
- Rosales-Ortega F. F., Kennicutt R. C., Sánchez S. F., Díaz A. I., Pasquali A., Johnson B. D., Hao C. N., 2010, *MNRAS*, **405**, 735
- Rowlands K., Gomez H. L., Dunne L., Aragón-Salamanca A., Dye S., Maddox S., da Cunha E., Werf P. v. d., 2014, *MNRAS*, **441**, 1040
- Saintonge A., et al., 2011, *MNRAS*, **415**, 32
- Saintonge A., et al., 2017, *The Astrophysical Journal Supplement Series*, **233**, 22
- Saintonge A., et al., 2018, *MNRAS*, **481**, 3497
- Salvatier J., Wiecki T. V., Fonnesbeck C., 2016, *PeerJ Computer Science*, **2**, e55
- Sánchez S. F., Rosales-Ortega F. F., Kennicutt R. C., Johnson B. D., Diaz A. I., Pasquali A., Hao C. N., 2011, *MNRAS*, **410**, 313
- Sandstrom K. M., et al., 2013, *ApJ*, **777**, 5
- Savage B. D., Sembach K. R., 1996, *ApJ*, **470**, 893
- Sawada T., et al., 2001, *The Astrophysical Journal Supplement Series*, **136**, 189
- Schön S., Kermarrec G., Kargoll B., Neumann I., Kosheleva O., Kreinovich V., 2018, in Anh L. H., Dong L. S., Kreinovich V., Thach N. N., eds, Econometrics for Financial Applications. Springer International Publishing, Cham, pp 266–275
- Scoville N., et al., 2014, *ApJ*, **783**, 84
- Sérsic J. L., Pastoriza M., 1965, *Publications of the Astronomical Society of the Pacific*, **77**, 287
- Sheather S. J., Jones M. C., 1991, Journal of the Royal Statistical Society. Series B (Methodological), **53**, 683
- Shetty R., Kauffmann J., Schnee S., Goodman A. A., 2009, *ApJ*, **696**, 676
- Slavin J. D., Dwek E., Jones A. P., 2015, *ApJ*, **803**, 7
- Smith M. W. L., et al., 2012, *ApJ*, **756**, 40

- Smith R. J., Glover S. C. O., Clark P. C., Klessen R. S., Springel V., 2014, *MNRAS*, **441**, 1628
- Smith M. W. L., et al., 2017, *The Astrophysical Journal Supplement Series*, **233**, 26
- Sparre M., et al., 2014, *ApJ*, **785**, 150
- Stein M. L., 1999, *Interpolation of Spatial Data: Some Theory for Kriging*, 1st edition edn. Springer, New York
- Sun J., et al., 2018, *ApJ*, **860**, 172
- Tabatabaei F. S., et al., 2014, *A&A*, **561**, A95
- Taylor M. B., 2005, in Shopbell P., Britton M., Ebert R., eds, *Astronomical Society of the Pacific Conference Series Vol. 347, Astronomical Data Analysis Software and Systems XIV*. p. 29
- Telford O. G., Werk J. K., Dalcanton J. J., Williams B. F., 2018, preprint, [p. arXiv:1811.02589 \(arXiv:1811.02589\)](https://arxiv.org/abs/1811.02589)
- Theil H., 1992, *A Rank-Invariant Method of Linear and Polynomial Regression Analysis*. Springer Netherlands, Dordrecht, pp 345–381, [doi:10.1007/978-94-011-2546-8_20](https://doi.org/10.1007/978-94-011-2546-8_20), https://doi.org/10.1007/978-94-011-2546-8_20
- Tremonti C. A., et al., 2004, *ApJ*, **613**, 898
- Usero A., et al., 2015, *AJ*, **150**, 115
- Utomo D., Chiang I. D., Leroy A. K., Sandstrom K. M., Chas-tenet J., 2019, *ApJ*, **874**, 141
- Valtchanov I., et al., 2017, *SPIRE Handbook. SPIRE Consortium and the SPIRE Instrument Control Centre*, 3.1 edn
- Vílchez J. M., Relaño M., Kennicutt R., De Looze I., Mollá M., Galametz M., 2019, *MNRAS*, **483**, 4968
- Walter F., Brinks E., de Blok W. J. G., Bigiel F., Kennicutt Jr. R. C., Thornley M. D., Leroy A., 2008, *AJ*, **136**, 2563
- Watson D., 2011, *A&A*, **533**, A16
- Weingartner J. C., Draine B. T., 2001, *ApJ*, **548**, 296
- Werner M. W., et al., 2004, *ApJS*, **154**, 1
- Whittet D. C. B., 1992, *Dust in the galactic environment*
- Wiseman P., Schady P., Bolmer J., Krühler T., Yates R. M., Greiner J., Fynbo J. P. U., 2017, *A&A*, **599**, A24
- Wolfire M. G., Hollenbach D., McKee C. F., 2010, *ApJ*, **716**, 1191
- Wong O. I., et al., 2006, *MNRAS*, **371**, 1855
- Wright E. L., et al., 2010, *AJ*, **140**, 1868
- York D. G., et al., 2000, *AJ*, **120**, 1579
- Young J. S., et al., 1995, *ApJS*, **98**, 219
- Ysard N., Jones A. P., Demyk K., Boutéraon T., Koehler M., 2018, *A&A*, **617**, A124
- Zafar T., Watson D., 2013, *A&A*, **560**, A26
- Zukovska S., 2014, *A&A*, **562**, A76
- da Cunha E., Charlot S., Elbaz D., 2008, *MNRAS*, **388**, 1595
- de Vaucouleurs G., de Vaucouleurs A., Corwin Jr. H. G., Buta R. J., Paturel G., Fouqué P., 1991, *Third Reference Catalogue of Bright Galaxies. Volume I: Explanations and references. Volume II: Data for galaxies between 0^h and 12^h. Volume III: Data for galaxies between 12^h and 24^h.*
- van der Walt S., Colbert S. C., Varoquaux G., 2011, *Computing in Science & Engineering*, **13**, 22

APPENDIX A: RADIAL METALLICITY PROFILE FITTING

The model we employed to fit the radial metallicity profiles of our target galaxies in Section 3.3 is described by the likelihood function:

$$\mathcal{L}(Z_i^{[\frac{O}{H}]} | R, \sigma, m_Z, c_Z, \psi) = \prod_i^n \left(\frac{1}{\sqrt{2\pi(\sigma_i^2 + \psi^2)}} \times \exp \left(-\frac{(Z_i^{[\frac{O}{H}]} - m_Z R_i - c_Z)^2}{2(\sigma_i^2 + \psi^2)} \right) \right) \quad (\text{A1})$$

where $Z_i^{[\frac{O}{H}]}$ is the $12 + \log_{10}[\frac{O}{H}]$ metallicity of the i^{th} datapoint, R_i is the deprojected galactocentric radius of the i^{th} datapoint (as a fraction of the R_{25}), m_Z is the metallicity gradient (in dex R_{25}^{-1}), c_Z is the central metallicity (in $12 + \log_{10}[\frac{O}{H}]$), ψ is the intrinsic scatter (in dex), and n is the number of datapoints.

We determined the posterior probability of our variables of interest – m_Z , c_Z , and ψ – in a Bayesian manner, sampling the posterior Probability Distribution Functions (PDF) using the PyMC3 (Salvatier et al. 2016) MCMC package for Python.

To inform the priors, we first performed a simple, preliminary least-squares fit, with only the gradient and central metallicity as free parameters. The priors on all three parameters then took the form of normal distributions. For c_Z , the mean of the prior was set to the central metallicity found by the preliminary least-squares fit, and the standard deviation on the prior was set to the standard deviation of all the input metallicity values. For m_Z , the mean of the prior was set to the gradient found by the preliminary least-squares fit, and standard deviation of the prior was set to the absolute value of the gradient found by the preliminary least-squares fit. For ψ , both the mean and standard deviation of the prior were set to the root-mean-square of the residuals between the input metallicity values and the preliminary least-squares fit.

APPENDIX B: UNCERTAINTIES ON GPR METALLICITY MAPPING

To determine the uncertainty of the GPR metallicity maps, we repeated the regression procedure 1000 times. For each iteration, we draw a random sample from the posterior PDF of our radial metallicity profile model, and used that sample to calculate the residual on each datapoint; we then applied the GPR to these residuals in the same manner as described above. For each iteration, the GPR produced a full posterior PDF for the predicted metallicity in each pixel (and by definition, Gaussian process regression yields Gaussian posterior PDFs).

Having repeated this process for the 1000 iterations, we had 1000 posterior PDFs for each pixel; these are then combined to give each pixel’s final metallicity PDF. To quantify the uncertainty in each pixel, we take the 63.3% quantile around the posterior median; these are the uncertainty values plotted in the lower-left panels of Figures 5 and 6. As can be seen, the uncertainty on the regression is low (< 0.05 dex) for pixels that have plenty of spectra metallicities; whilst for pixels more distant from any spectra, making the predicted values more dependent upon extrapolation, the uncertainty is much larger (> 0.25 dex). Indeed, for pixels with few or no spectra metallicities in the immediate vicinity, relying upon the metallicity predicted by a 1-dimensional globally-fitted gradient could provide a false sense of confidence – especially in M83, where the metallicity data is concentrated in a central band. We therefore argue that in these areas, the larger uncertainties predicted by our GPR approach are likely to be more realistic.

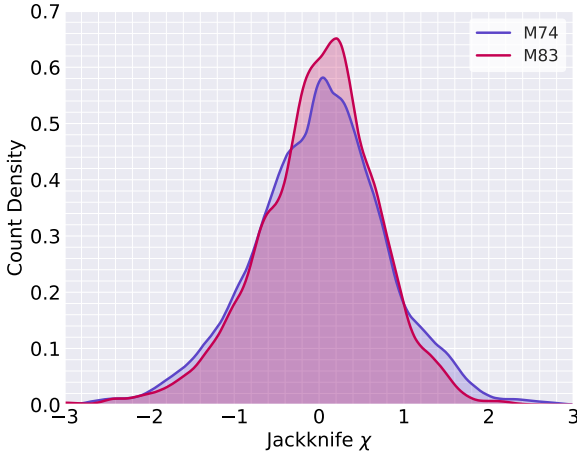


Figure C1. Distribution of χ values found for our jackknife cross-validation of the GPR metallicity mapping. Distributions plotted as Kernel Density Estimates (KDEs), using an Epanechnikov kernel, with bandwidth calculated using the Sheather-Jones rule (Sheather & Jones 1991).

APPENDIX C: VALIDATION OF GPR METALLICITY MAPPING

To verify that our GPR metallicity mapping technique is reliable, and not generating spurious features in the final metallicity maps, we used a Monte Carlo jackknife cross-validation analysis. For this, we performed 500 repeats of the GPR metallicity mapping; for each repeat, half of the spectra metallicity points were selected at random to be excluded from the fitting, to serve as a control sample for later reference. The GPR was then computed using the remaining half of the points (but otherwise following the modelling process as laid out above). By comparing the metallicity values of the masked spectra to the metallicities predicted by the GPR method at their positions, we can evaluate the accuracy of the generated metallicity maps.

For each of the 500 jackknife iterations, we found the deviations between the known metallicities of the control spectra, and the metallicity predicted by the GPR at those positions. We assessed the deviation at each position in terms of χ , defined as:

$$\chi = \frac{Z_{GPR}^{[O/H]} - Z_{spec}^{[O/H]}}{\sqrt{\left(\sigma_{GPR}^{[O/H]}\right)^2 + \left(\sigma_{spec}^{[O/H]}\right)^2}} \quad (C1)$$

where $Z_{GPR}^{[O/H]}$ is the metallicity predicted by the GPR at the position in question, $Z_{spec}^{[O/H]}$ is the actual metallicity of the spectra, $\sigma_{GPR}^{[O/H]}$ is the uncertainty on the GPR at the position in question, and $\sigma_{spec}^{[O/H]}$ is the uncertainty on the spectra metallicity (all Z and σ terms expressed in $12 + \log_{10}[\frac{O}{H}]$ units). In short, χ expresses the deviation in terms of the mutual uncertainty on the spectra metallicity and the GPR.

If the metallicities predicted via GPR suffer from no systematic offset, then the mean χ should be $0 \pm n^{-\frac{1}{2}}$ (where n is the number of control spectra). Similarly, if the uncertainties on the GPR metallicities are Gaussian and accurate, then 68.3% of the values of χ should lie in the range $-1 < \chi < 1$.

The distribution of jackknife χ values we find for both

galaxies are shown in Figure C1. The distributions are symmetric, near-Gaussian, and centred close to zero. The mean jackknife χ values are 0.0079 ± 0.0029 and -0.0057 ± 0.0023 for M74 and M83 respectively. These offsets are $> 2\sigma$, suggesting that there tends to be a small systematic offset (positive for M74, and negative for M83) between the metallicity predicted by the GPR, and the actual metallicity of the spectra. But whilst technically significant, these systematic offsets are nonetheless vanishingly small in terms of actual metallicity – the mean jackknife deviation in $12 + \log_{10}[\frac{O}{H}]$ units is 0.00056 for M74, and -0.00037 for M83. We are satisfied that systematic effects at this scale are minute enough to have no appreciable impact on any of our results.

For M74, 80.5% of the jackknife χ values lie in the $-1 < \chi < 1$ range; for M83 the fraction is 85.4%. These are both somewhat larger than the expectation of 68.3%, which suggests that our GPR maps are actually somewhat *more* precise than suggested by their uncertainties. In other words, it appears that the GPR uncertainties are overestimated by factors of approximately 1.18 and 1.25 (for M74 and M83 respectively) – a small enough difference that we judge it unnecessary to attempt a *post-hoc* fine-tuning of the output uncertainties.

Additionally, see the discussion in Section 6.1 of the effect of the metallicity maps upon our resulting maps of κ_d .

APPENDIX D: DUST SED PRIORS

Our SED-fitting procedure, detailed in Section 4.2, has 6 free parameters: dust temperature, T_d ; dust ‘mass’ normalisation, $M_d^{(norm)}$; emissivity slope, β ; and correlated photometric error in the *Herschel*-SPIRE bands, v_{SPIRE} . The prior probability distributions for all these free parameters are shown in Figure D1.

D1 Temperature Prior

The prior on temperature is given by a standardised⁴² gamma distribution of the form:

$$\mathcal{P}(T) = \frac{\left(\frac{T-l}{s}\right)^{\alpha-1} \exp\left(-\frac{T-l}{s}\right)}{s \Gamma(\alpha)} \quad (D1)$$

where T_d is the temperature, l is the location parameter, s is the scale parameter, and α is the shape parameter. The location parameter l functions such that $\mathcal{P}(T < l) = 0$. We define the scale parameter in relation to the distribution mode \tilde{T} (ie, the temperature with the peak prior probability), according to:

$$s = \frac{\tilde{T} - l}{\alpha - 1} \quad (D2)$$

where, for our T_d prior, these parameters take values of $\alpha = 2.5$, $l = 5$, and $\tilde{T} = 20$.

For T_d , the modal value of 20 K corresponds to the approximate average of the cold dust temperatures seen

⁴² Standardised as per the SciPy (Jones et al. 2001) gamma distribution implementation: <https://docs.scipy.org/doc/scipy/reference/generated/scipy.stats.gamma.html>

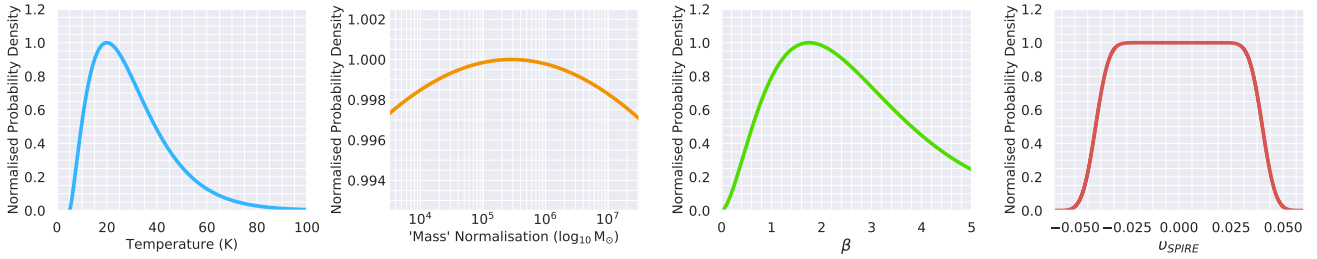


Figure D1. Prior probability distributions for T_d , $M_d^{(\text{norm})}$, β , and v_{SPIRE} . For ease of viewing and comparison, all distributions have been normalised so that they peak at a probability density of 1. The prior for $M_d^{(\text{norm})}$ is computed for each source (eg, pixel) based on its brightness and distance; the exemplar distribution displayed in the upper-right panel is for the pixel in M83 centred at $\alpha = 204.2841^\circ$, $\delta = -29.8559^\circ$.

in nearby galaxies, in both global (Galametz et al. 2012; Clemens et al. 2013; Ciesla et al. 2014) and resolved (Smith et al. 2012; Gordon et al. 2014; Tabatabaei et al. 2014) analyses. Across the 13–30 K temperature range, $\mathcal{P}(T_c) > 0.8\mathcal{P}(\tilde{T}_c)$; this corresponds to range spanned by the lower cold dust temperatures seen in blue dust- and gas-rich galaxies (Clark et al. 2015; Dunne et al. 2018), to the higher cold dust temperatures seen in dust-poor dwarf galaxies (Rémy-Ruyer et al. 2013; Izotov et al. 2014). In other words, temperatures across this ‘standard’ temperature range are only slightly less favoured than \tilde{T}_c . Outside this range, there is an increasing penalty – especially towards lower temperatures, where $\mathcal{P}(T_c < 5) = 0$, to rule out unphysically cold dust.

D2 Mass Prior

As described in Section 4.2, our SED fitting procedure uses an arbitrary placeholder value of κ_d (because the whole purpose of the SED fitting is to *find* values of κ_d); as a result, the ‘mass’ variable being fitted simply serves as a normalisation parameter.

Our mass normalisation prior takes the form of a 1st-order (ie, 1 degree of freedom) Student t distribution, constructed in base-10 logarithmic space (see Figure D1), with widths of $\sigma = 10$ dex. The peak of the mass normalisation prior is computed separately for each source (eg, pixel), based on its distance and brightness, according to the formula:

$$\log_{10}(\tilde{M}) = \log_{10}(S_{\text{max}}D^2) + \left(\frac{\tilde{T} - 20}{-15}\right) + 4 \quad (\text{D3})$$

where $\tilde{M}^{(\text{norm})}$ is the modal mass of the prior probability distribution, S_{max} is the brightest flux measured in the 150–1000 μm range (in Jy), and D is the source distance (in Mpc). For MBB dust SEDs with temperatures in the 15–25 K range, the brightest flux in the *Spitzer* and *Herschel* bands will be the 160 μm measurement.

Equation D3 is a purely empirical relation, derived from the SED fitting of *Herschel* Reference Survey (Boselli et al. 2010) galaxies, as performed in Clark et al. (2015) and Clark et al. (2016).

The prior on $M^{(\text{norm})}$ shown in Figure D1 is for an example pixel from our M83 data (processed as per Section 4.1), centred at $\alpha = 204.2841^\circ$, $\delta = -29.8559^\circ$. The brightest band for this pixel is 160 μm , where the flux is 1.18 Jy. Given a distance to M83 of 4.9 Mpc, that corre-

sponds to a priors centred at $\tilde{M}^{(\text{norm})} = 5.45 \log_{10} M_\odot$, as per Equation D3.

The mass normalisation prior is designed to be very weak. This is because the strong $M \propto T^{4+\beta}$ dependence of mass on temperature (for a given luminosity) means that the fitted value of the mass normalisation term is often driven primarily by the fitted temperature.

D3 β Prior

The prior on β takes the form of a standardised gamma distribution, identical to Equations D1 and D2, except with β replacing T_d , and $\tilde{\beta}$ replacing \tilde{T} . The parameters for our β prior take values of $\alpha = 2.75$, $l = 0$, and $\tilde{\beta} = 1.75$.

For nearby galaxies and the Milky Way, β is typically found to lie in the range 1.5–2.0, with resolved analyses finding values spanning 1.0–2.75 (Smith et al. 2012; Kirkpatrick et al. 2013; Planck Collaboration et al. 2014). We therefore construct our prior such that it peaks at $\tilde{\beta} = 1.75$, with $\mathcal{P}(\beta) > 0.8\mathcal{P}(\tilde{\beta})$ across the 1.0–2.75 range. To exclude dubiously-physical low β values, $\mathcal{P}(\beta < 0) = 0$.

D4 v_{SPIRE} Prior

As discussed in Section 4.2, the calibration uncertainties on *Herschel*-SPIRE photometry has a correlated systematic error component, which we term v_{SPIRE} , arising from uncertainty on the emission model of Neptune, the instrument’s primary calibrator. v_{SPIRE} has a value of $\pm 4\%$; the true value of the systemic error is believed to be equally likely to lie anywhere in that range, with minimal likelihood ($\sim 5\%$) of the value lying outside it (Bendo et al. 2013; A. Papageorgiou, *priv. comm.*; C. North, *priv. comm.*).

We therefore use a prior for v_{SPIRE} that takes the form of a boxcar function convolved with a Gaussian distribution. The boxcar function has a value of 1 over the range -0.04–0.04, with a value of 0 beyond this. The Gaussian with which it was smoothed has a standard deviation of 0.005. In the resulting prior, as shown in the lower-right panel of Figure D1, 95% of the probability density is contained within the -0.04–0.04 range.

APPENDIX E: κ_d MAPS AT 160 μm

As discussed in Section 5, we calculated our κ_d maps at a reference wavelength of 500 μm . This is the longest wave-

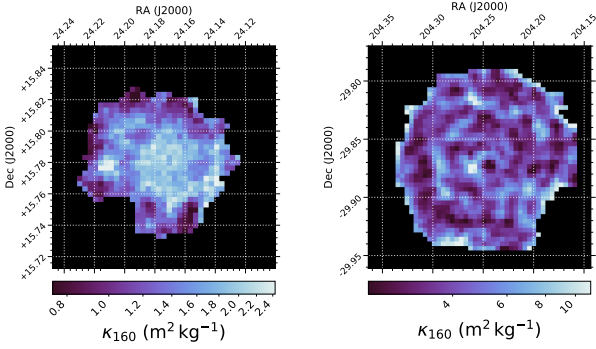


Figure E1. Maps of κ_{160} within M74 (left) and M83 (right).

length at which we have data, making it less sensitive to uncertainties in temperature derived from the SED fitting. However, many authors opt to present κ_d at 160 μm , as this is the wavelength regime at which the κ_d of carbonaceous and silicate dust is most comparable.

For completeness, we therefore also produced κ_{160} maps, which are shown in Figure E1. The maps are noisier than those computed at 500 μm , but the overall morphology of κ_{160} in both galaxies is nonetheless the same as that of κ_{500} .

Using the same independent-pixel non-parametric bootstrap approach as in Section 5, we find a median underlying range of κ_{160} values of 0.74–2.4 $\text{m}^2 \text{kg}^{-1}$ for M74 (a factor of 3.2 variation), and 2.1–12 $\text{m}^2 \text{kg}^{-1}$ for M83 (a factor of 5.7 variation).

APPENDIX F: κ_{500} MAPS USING DIFFERENT STRONG-LINE METALLICITY PRESCRIPTIONS

As described in Section 3.3, our metallicity maps were produced using metallicities calculated using the ‘S’ strong-line prescription of Pilyugin & Grebel (2016). To ensure that our specific choice of metallicity prescription wasn’t driving our results, we also repeated our κ_{500} mapping using metallicity maps produced using 4 other strong-line prescriptions; the O3N2 prescription of Pettini & Pagel (2004), the N2 prescription of Pettini & Pagel (2004), the prescription of Tremonti et al. (2004), and the IZI prescription of Blanc et al. (2015). As with our fiducial Pilyugin & Grebel (2016) ‘S’ prescription values, these metallicities are all taken from the standardised database produced by De Vis et al. (2019). The resulting κ_{500} maps for all 4 prescriptions for both galaxies are presented in Figures F1 and F2. These κ_{500} maps all display the same general morphology as the fiducial maps in Figures 12 and 13 – with lower values of κ_{500} associated with regions of denser ISM. The exceptions to this are the maps produced using the Tremonti et al. (2004) prescription, which causes a negative radial gradient in κ_{500} to dominate over the density-anticorrelated variations; but nonetheless, at a given radius, areas of lowest κ_{500} are associated with the same areas of denser ISM as seen in the other maps.

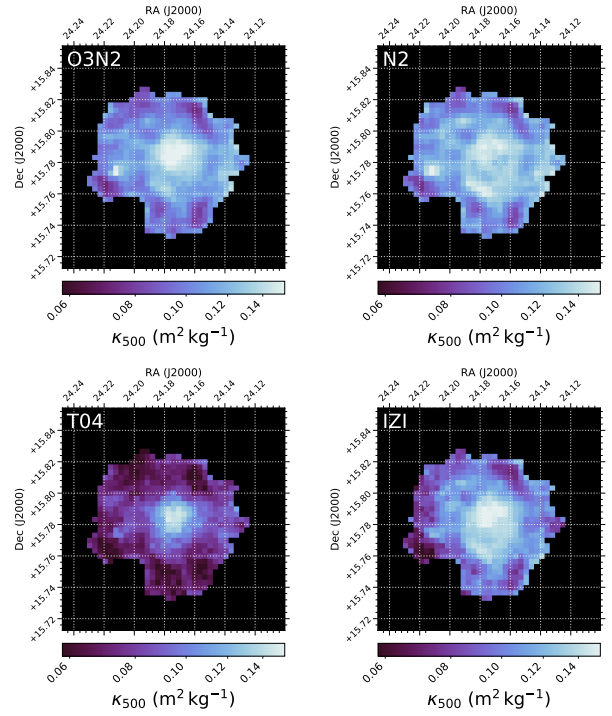


Figure F1. Maps of κ_{500} within M74, calculated using metallicities produced via different strong-line prescriptions. Upper left: the O3N2 prescription of Pettini & Pagel (2004). Upper right: The N2 prescription of Pettini & Pagel (2004). Lower left: The prescription of Tremonti et al. (2004). Lower right: the IZI prescription of Blanc et al. (2015).

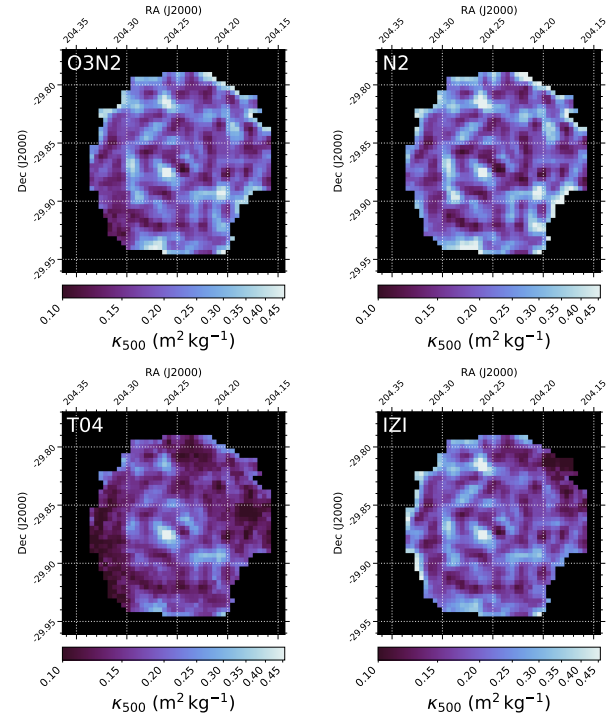


Figure F2. Maps of κ_{500} within M83, calculated using metallicities produced using different strong-line prescriptions, but otherwise following the same method as for our fiducial map in Figure 13. Prescription descriptions the same as for Figure F1.

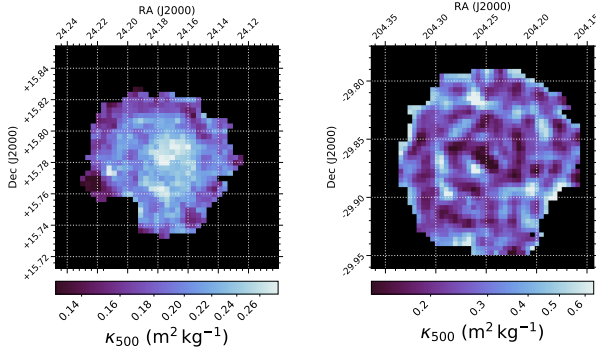


Figure G1. Maps of κ_{500} within M74 (*left*) and M83 (*right*), produced when the FIR–submm SED is modelled with a two-component MBB, as opposed to the one-component MBB used for our fiducial maps.

APPENDIX G: κ_d MAPS FROM TWO-COMPONENT MBB SEDS

As discussed in Section 4.2, we opt to use a one-component MBB model to fit the FIR–submm SEDs for our fiducial κ_{500} maps. However, as a test, we also produced κ_{500} maps using a two-component MBB model for the SED fitting. In practice, this entailed replacing Equation 9 with:

$$S_{d_i} = \frac{\kappa_0}{D^2} \left(\frac{\lambda_0}{\lambda_i} \right)^\beta \left(M_c^{(\text{norm})} B(\lambda_i, T_c) + M_w^{(\text{norm})} B(\lambda_i, T_w) \right) \quad (\text{G1})$$

where subscripts c and w denote the cold and warm dust components respectively. There are therefore 6 free parameters for the two-component MBB modelling: T_c , $M_c^{(\text{norm})}$, T_w , $M_w^{(\text{norm})}$, β , and v_{SPIRE} . Having performed this SED fitting, computing the corresponding values of κ_{500} simply requires setting $n = 2$ in Equation 3 and providing T and S_λ for both MBB components.

Expanding the method to incorporate two dust components includes the tacit assumption that both dust components have the same dust-to-metals ratio. This is perhaps unlikely, as warmer dust will generally be associated with recent star formation and more intense ISRFs, where shocks and high-energy photons might destroy grains and return their metals to the gas phase. However, for dust SEDs with two distinct components at different temperatures, the total dust mass is invariably dominated by the colder component (da Cunha et al. 2008; Kirkpatrick et al. 2014; Clark et al. 2015); therefore the resulting value of κ_d will primarily reflect the κ_d of the dominant component, insulating this approach against differences in ϵ_d .

The resulting maps are shown in Figure G1. The map for M74 shows some increase in κ_{500} in the centre relative to the one-component MBB approach, whilst the map for M83 is practically identical.

The median for M74 is $\kappa_{500} = 0.20 \text{ m}^2 \text{ kg}^{-1}$, and the median for M83 is $\kappa_{500} = 0.25 \text{ m}^2 \text{ kg}^{-1}$. The ranges of values (estimated via same the non-parametric independent-pixel bootstrap method as used in Section 5) are $0.13\text{--}0.28 \text{ m}^2 \text{ kg}^{-1}$ for M74 (a factor of 2.2 variation), and $0.12\text{--}0.72 \text{ m}^2 \text{ kg}^{-1}$ for M83 (a factor of 6.0 variation). The differences between these values and their counterparts for our fiducial maps are all much less than the average 0.15 dex

statistical uncertainty on each pixel’s κ_{500} value (and well within the 0.2 dex systematic uncertainty).